MASTER

Multiphysics modelling of Ionic Polymer-Metal Composite actuators with the Finite Element Method

de Reuver, H.A.

Award date:
2021

EINDHOVEN UNIVERSITY OF TECHNOLOGY

Department of Mechanical Engineering
Research Group ET
Groene Loper, 5612 AE Eindhoven
The Netherlands
www.tue.nl

Author
Henk A. de Reuver

Supervisors
dr.ir. Rick C. de Lange
dr.ir. Joris J.C. Remmers
Eva A. Sideris, MSc.

Date
April 7, 2021

Multiphysics modelling of Ionic Polymer-Metal Composite actuators with the Finite Element Method

A thesis submitted for the degree of Master of Science in Mechanical Engineering

Henk A. de Reuver ID: 0892382
h.a.d.reuver@student.tue.nl

Abstract

Ionic Polymer-Metal Composites are emerging as soft, smart, electromechanical actuators that can be used in devices such as linear peristaltic pumps. The pump in question uses a monolithic actuator, machined to have multiple actuation units. For optimisation of its performance, stress-relief slits are cut between actuation units in kirigami-like patterns. Due to the complex geometries in which this results, further optimisation requires a numerical model to perform design studies with.
In this work a grey-box, electromechanical model was used to compose a IPMC-plate FEM element which was implemented in a FEM framework. The mechanical aspects of the new element are derived from the Plate Theory since this fits the sheet-like shape of IPMC material. The plate curvature was made dependent on charge, calculated via a Transmission Line model of the IPMC, establishing electromechanical coupling. Thereafter, the physics of the element was numerically verified by analysing problems with known solutions. This included limit cases with respect to the electronic degree of freedom and tests for convergence. Furthermore simulation results were shown of complex, monolithic actuators, representative of those driving the peristaltic pump, as proof-of-concept for the new element. additionally, it was shown that performance, in terms of displacement and stresses, could be qualitatively analysed. The work was concluded by demonstrating the effectiveness of kirigami patterns with a comparison between actuators with and without the kirigami slits.

EINDHOVEN UNIVERSITY OF TECHNOLOGY

Table of contents

Title
Multiphysics modelling of Ionic Polymer-Metal Composite actuators with the Finite Element Method

EINDHOVEN UNIVERSITY OF TECHNOLOGY

Table of contents

Title
Multiphysics modelling of Ionic Polymer-Metal Composite actuators with the Finite Element Method

1 Introduction

Ionic Polymer-Metal Composites (IPMC) are a composite material comprised of a thin membrane of Electroactive Polymer (EAP) plated with metal electrodes on its surfaces [13]. When electronically stimulated, an IPMC will bend according to the distribution of voltage across its metal electrodes. What sets IPMCs apart from other electromechanic materials, such as piezoelectric ones, is the fact that the material itself is soft. Furthermore, IPMCs are capable of deforming to higher strains, by as much as two orders of magnitude greater, and are capable of doing so for lower drive voltages[6].

The membrane polymer has anions fixed in its configuration. These anions are balanced by hydrated, mobile, cations in the liquid that the IPMC is wetted in. The electrodes on the surface of the IPMC serve to conduct electrons from one point on the surface of the sheet to another.
The uses of such a composite material are either as electromechanical actuator or sensor. In sensor mode a potential difference is generated by deformation of the IPMC whereas in actuation mode, a potential difference is posed over the electrodes.
The applied voltage causes the hydrated cations to be attracted to the negative electrode and redistribute themselves accordingly. Together with the cations, the water molecules migrate towards the anode. This results in the polymer network expanding near the anode and contracting near the cathode [7]. The combined swelling and shrinking of the polymer induces curvature to the sheet of IPMC, bending it. A schematic representation of the construction and working principle of IPMCs is shown in Figure 1.1. It shows that water and cations are homogeneously distributed in an IPMC in rest and non-homogeneously distributed when provided with a potential difference.

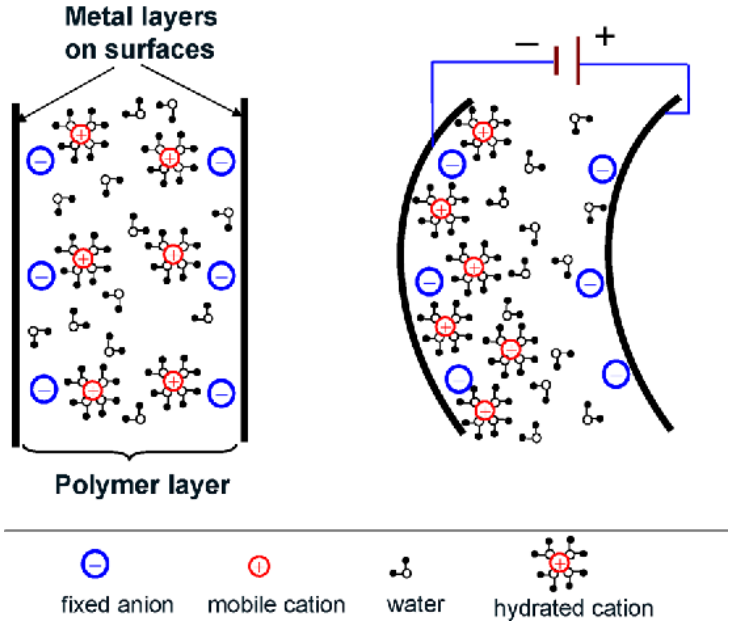

Figure 1.1: Schematic representation of the electromechanical coupling in IPMC material [9].

In sensor mode, the IPMC sheet is bent by external, mechanical loads. Due to this bending, mobile particles are displaced from the region loaded in compression to the region loaded in tension; from one electrode to the other. As a result of the unequal anion-cation distribution, a potential difference is posed on the electrodes and a small current may be produced [8].

In prior research a linear peristaltic pump was made driven by a monolithic IPMC actuator [17]. The pump moves fluid by means of a membrane excited by a traveling wave, driven by the IPMC actuator. The actuator itself was made from a Nafion membrane plated with platinum electrodes.

In order to manufacture the monolithic actuator, one sheet of IPMC material is worked to create eight mechanically attached but separately operating IPMC actuating units. In order to create these separate units, the electrodes on the surfaces are electronically decoupled by etching away some of the metal with laser micromachining methods.
Furthermore, stress relieving, kirigami-inspired slits are cut through the sheet to increase the magnitude of curvature of the actuation units, increasing pumping efficiency. Additionally, holes are machined through the actuation units such that a water tight membrane can be attached. The complete actuator design is shown in Figure 1.2 where blue indicates intact IPMC material, white etched IPMC material and grey removed IPMC material.

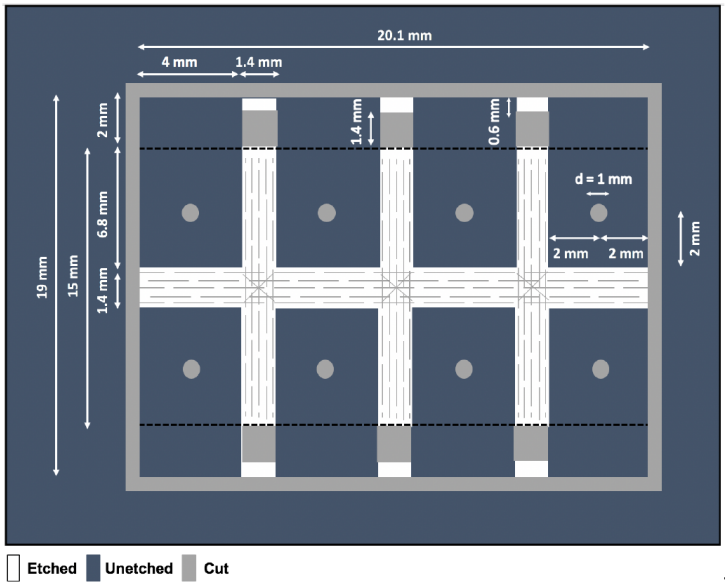

Figure 1.2: Design of the distributed IPMC actuator for use in a linear peristaltic microfluidic pump in top view. Etched areas are represented in white, the IPMC actuator units are colored in dark grey and cuts and holes in light grey [17]

The IPMC actuator still requires optimisation, mostly in the kirigami pattern, to increase pumping efficiency. The problem is that the complex geometry of the actuator makes it difficult to make predictions on the performance for variations in the design; a numerical approach is needed.
The goal of this project is to make a numerical simulation tool that is capable of modelling the electromechanical behaviour IPMC actuators. Furthermore, it must be able to handle complex geometries such as the one described above, with the purpose to analyse the effect of variations in design to the performance of the actuator. The numerical model is to use the Finite Element Method (FEM) since it is well suited for complex geometries.

The first step towards the final product is to select a model for the electrical response of the IPMC to applied electric loads from the literature. The output of the electric model then has to interact with a separate mechanical model to translate applied electric load into deformation of the geometry. The two selected models and their governing equations are introduced in Chapter 2.
The second step is to convert the models from the literature into a suitable format for the Finite Element approach; into a matrix-vector system of equations. The required steps and mathematical operations are explained, from start to finish, in Chapter 3.
Next is to implement these systems of equations into a FEM framework. This framework is responsible for the administration of all geometrical and parametric inputs, for the assembly of a single system of equations from these inputs combined with the electric and mechanical models and for producing an organized array of outputs. A readily available, open-source FEM code[3] was used as explained at the

end of Chapter 3.
Once implemented, it is important to verify that the numerical results are accurate and reliable and that the model can handle complex geometrical features. To this end, an IPMC actuator is modelled and simulations are performed with varying material parameters and simulation settings. The numerical results are compared to analytical results for accuracy and tested for convergence for reliability. This results of this process is provided in Chapter 4.
The final part of this work is a presentation of use cases of the multiphysics FEM simulations. Proof is shown that the intended simulations, for which this model was made, can be performed and analysed. These simulations and their results are shown in Chapter 5.

2 IPMC Modelling

In order to model an IPMC actuator, the material behaviour is subdivided into an electric module and a mechanical module. To this end, the IPMC material must be given an electric degree of freedom on top of its mechanical degrees of freedom. The two modules need to be coupled such that the mechanical degrees of freedom are dependent on the electric degree of freedom.
The electric degree of freedom and its governing equations are derived in Chapter 2.1 of this report. The mechanical degrees of freedom and their governing equations and, more importantly, the electromechanical coupling are explained in Chapter 2.2 of this report.

2.1 Electronic behaviour

Models for the electric behaviour of IPMCs are available as black-box [14], grey-box [4] [11] and white-box [5] [12] models. The black-box models tend to be described in the frequency domain due to the system identification tools used whereas white-box models are described in the time domain as these are derived from theory.
Since the model in this work is to be implemented into a FEM framework, we require it to be described in the time domain. Furthermore, since the priority is to obtain good qualitative results, a grey-box modelling approach is selected.
This model describes the response of a material to electric inputs with a circuit of resistors, conductors and capacitors [11]. This representative electric circuit models the electric properties of the IPMC material from electrode to electrode.

The unit circuit in this work consists of a capacitor (C) placed in series with a conductor (W). In parallel with these two components is another conductor (G). Capacitor C introduces the time-dependent behaviour of the electric response, characteristic of IPMCs. Each unit circuit is connected to the electric input via a series of surface resistors (Ra and Rb).
Figure 2.1 shows the electric layout of a sheet of IPMC material in side-view. Note that the array of unit circuits resembles a Transmission Line problem; a well-documented topic in Electrical Engineering for which analytical solutions are readily available.

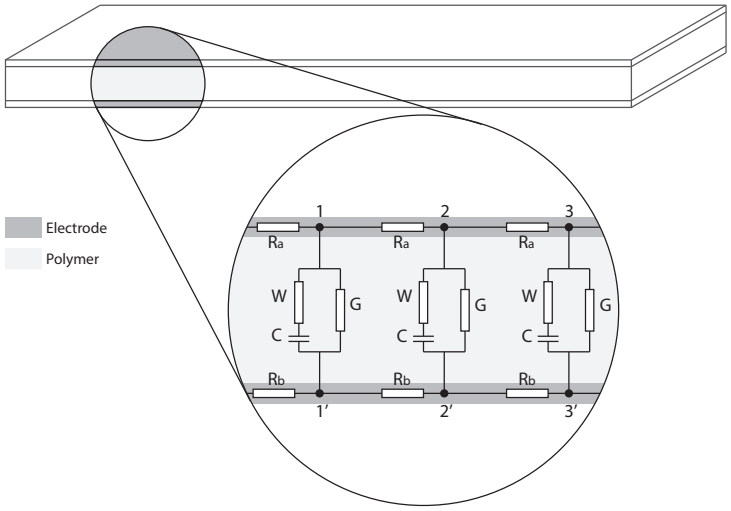

Figure 2.1: IPMC material represented by a series of representative electric circuits.

In this unit circuit, each component can be attributed to a physical phenomenon. Starting with resistors R_a and R_b; these can be attributed to the conductivity of the electrodes. They are dependent on the type of material used and the geometry of the electrodes. The effect of surface resistance can be observed by

the rate with which the induced curvature decreases with distance from the applied potential difference. The capacity of capacitor C is a measure for how many cations can be accumulated near the anode as well as the ionic charge of the accumulated cations. Its effect can be observed through the maximum deflection of the IPMC actuator
The conductor W is then closely linked to the mobility of these cations. The less resistance in their path through the polymer, the quicker they allow for the accumulation of cations near the anode. The effect of W is observed through the deformation rate of the IPMC actuator.
Conductor G can be attributed to the current flowing between electrodes without performing work on the cations; it causes a loss of energy.

2.1.1 Electric potential

From the transmission line problem identified in the previous section as presented in Figure 2.1, we may obtain a differential equation. In particular, the partial differential equation for the potential difference over the surfaces of the IPMC can be obtained for the one-dimensional case [11] as:

$$C\frac{\partial^3 p}{\partial x^2 \partial t} + W\frac{\partial^2 p}{\partial x^2} - R(G+W)C\frac{\partial p}{\partial t} - RGWp = 0 \tag{2.1}$$

It describes the electric potential difference (p), in space and time, over the electrodes ($1-1'$, $2-2'$, $\ldots$, $n-n'$) of the IPMC. Parameters C, W, and G represent the electric components from Figure 2.1 and $R = Ra + Rb$.

In order to extend the differential equation to two dimensions we use the fact that the plated electrodes are metallic, making them inherently isotropic. Furthermore, since the polymer membrane is already assumed to have constant out-of-plane properties over the first in-plane direction, we simply extend that assumption to the second. Using these properties, Equation 2.1 can therefore be interpreted as a two-dimensional equation with $x = x(x, y)$.

2.1.2 Charge

With potential difference p, obtained in the previous section, across the electrodes we can isolate the series RC circuit with conductor W and capacitor C and analyse them separately from the rest of the representative electric model. Figure 2.2 shows the observed electric circuit with voltage $p(t)$ as the solution from Equation 2.1, W the conductivity of the resistor and C and q the capacitance and charge on the capacitor, respectively.

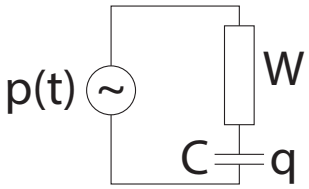

Figure 2.2: The RC circuit to charge capacitor C from the representative electric model with $p(t)$ the potential difference over the electrodes of the actuator.

From the circuit of Figure 2.2, using Kirchhoff's voltage law, we obtain that electric potential $p(t)$ is equal to the sum of the voltage drop over conductance W and the voltage drop over capacitor C. This yields an equation with potential, current and charge as:

$$p(t) = \frac{i(t)}{W} + \frac{q(t)}{C} \tag{2.2}$$

where $i(t)$ is the current through the circuit as a result of $p(t)$.

Using the definition of current, charge per second, we find that the current through C is equal to the change in charge over time and obtain a differential equation for charge as:

$$CWp(t) = C\frac{dq}{dt} + Wq(t) \tag{2.3}$$

2.1.3 Analytical solutions of limit cases

As a way to check the obtained equations for potential and charge, we mathematically investigate cases where one of the parameters of the representative electric circuit R, C, W or G approaches either zero or infinity. For each of these limit cases we can provide the analytical solutions to the potential and charge fields.

First we investigate the case in which the surface resistance of the IPMC is reduced to zero. Physically this could mean that the electrodes are so thick and conductive that their resistance becomes completely negligible with respect to conductors W and G.
Given that $R = 0\ \Omega\ \text{mm}^{-1}$, Equation 2.1 reduces to:

$$\frac{\partial}{\partial t}\left(\frac{\partial^2 p}{\partial x^2}\right) + \frac{W}{C}\frac{\partial^2 p}{\partial x^2} = 0 \tag{2.4}$$

Where, due to the absence of surface resistance, the potential is no longer dependent on the spacial dimensions such that:

$$\frac{\partial p}{\partial x} = 0, \qquad \frac{\partial^2 p}{\partial x^2} = 0 \tag{2.5}$$

The solution to this problem is a uniform potential difference across the entire IPMC. This also removes spatial dependence from the charge field even though the equation for charge does not reduce. Additionally, note that while the potential difference is no longer time dependent, the charge still is.

Secondly, we investigate the case in which capacitance of the IPMC reduces to zero. Physically, this could mean that there are no mobile ions throughout the polymer and any ions that are present are not separated.
Given that $C = 0\ \text{mF mm}^{-1}$, the equations for potential and charge reduce to:

$$\begin{aligned} \frac{\partial^2 p}{\partial x^2} - RGp &= 0 \\ q &= 0 \end{aligned} \tag{2.6}$$

The solution to the potential field has become independent of time and should result in an exponential decay in space away from the constrained boundary. This potential difference does not, however, result in any charge in the capacitor.

Thirdly, we investigate the case in which the capacitive conductance of the IPMC reduces to zero. The physical meaning of this could be that there are no mobile ions throughout the polymer. There can, however, exist a separation in the fixed anions and cations such that there is a constant dipole.
Given that $W = 0\ \Omega^{-1}\text{mm}^{-1}$, Equations 2.1 and 2.3 are reduced to:

$$\begin{aligned} \frac{\partial^2 p}{\partial x^2} - RGp &= 0 \\ \frac{dq}{dt} &= 0 \end{aligned} \tag{2.7}$$

Note that this yields the same solution to the potential difference as the case of zero capacitance. This is to be expected since neither case allows current to pass capacitor C. Therefore the charge in the capacitor remains in its initial state which, notably, is not necessarily fully discharged.

Finally, we investigate the case in which the conductance of the IPMC membrane approaches infinity. Physically, this means that the polymer is electrically highly conductive and thus bypasses current past the capacitor; a short circuit.
Given that $G \to \infty\ \Omega^{-1}\text{mm}^{-1}$, Equation 2.1 reduces to:

$$\frac{\partial p}{\partial t} + \frac{W}{C}p = 0 \tag{2.8}$$

Where, due to the short circuit condition, no potential difference between electrodes is possible such that:

$$p = 0 \tag{2.9}$$

In which case Equation 2.3 reduces to:

$$C\frac{dq}{dt} + Wq(t) = 0 \tag{2.10}$$

The solution to this problem is no potential difference between electrodes anywhere on the IPMC except on the constrained boundaries. This solution is temporally constant. The solution to the charge shows an exponential decay in time towards the fully discharged state, if it were initially charged.

2.2 Mechanical behaviour

Now that we have introduced the electrical behaviour of IPMCs, we can put our attention to the mechanical behaviour of the material. We begin by making the observation that a sheet of IPMC material is usually thin. So thin, in fact, that it is not necessary to model the out-of-plane dimension of the sheet explicitly[2]. Reducing the modelling space from three to two dimensions certainly lowers computational costs. A mathematical model fitting this description is the Plate Theory, derived from the mathematical description of beams [2]. Additionally, due to the lack of an out-of-plane dimension, the representative electric circuits, which connect surface to surface, are contained in a single element. This makes solving for the electric degree of freedom simple.

In this chapter we will start from a free body diagram and derive expressions for the force equilibrium in each of the three dimensions. Note that the out-of-plane dimension is included since loads may be exerted on the two-dimensional plate in this direction.
From a second free body diagram, we will derive two more equilibrium equations; those for the moments about the two in-plane directions.
These resulting five differential equations govern the deformation of the IPMC sheet in its five mechanical degrees of freedom: translation in three dimensions and rotation about the in-plane axes.

2.2.1 Force equilibrium equations

Beginning with the force equilibrium equations of an object, we usually start with a free-body diagram. Therefore, we introduce Figure 2.3 showing an infinitesimal IPMC plate element subjected to internal shear and normal forces, $\mathbf{Q}$ and $\mathbf{N}$ respectively. On top of that is an external load $\mathbf{F}$ with components in all three dimensions. The plate element in question has small deflections with angles α_x and α_y in the in-plane directions x and y respectively.

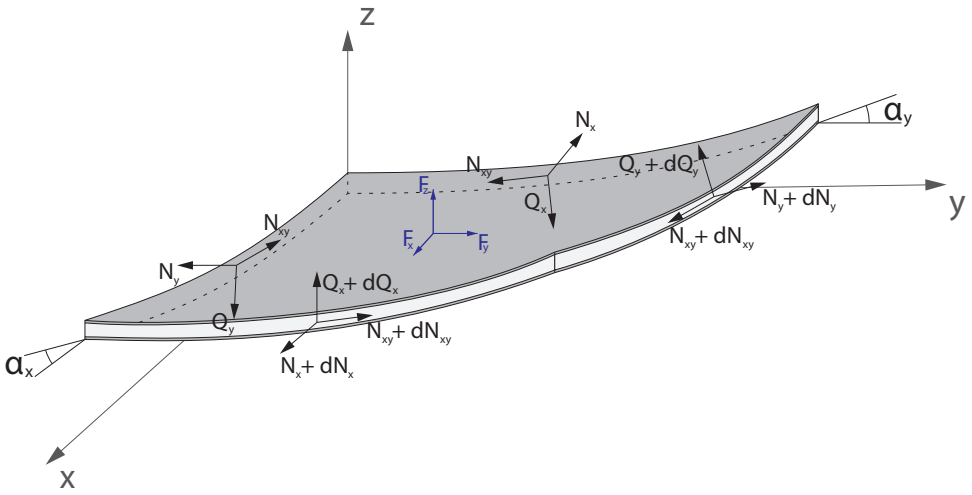

Figure 2.3: An infinitesimal IPMC plate element with deflection angles α_x and α_y and its internal shear and normal forces $\mathbf{N}$ and $\mathbf{Q}$, respectively. Adapted from: [10]

The complete derivation of the force equilibrium equations, starting from the free body diagram up to the differential equations, can be found in Appendix A. Only the resulting differential equations are given in the remainder of this chapter.

From the force equilibrium in x-direction, the following differential equation is obtained:

$$\frac{\partial N_x}{\partial x} + \frac{\partial N_{xy}}{\partial y} + F_x = 0 \tag{2.11}$$

Similarly, the force equilibrium in y-direction leads to the second equilibrium equation:

$$\frac{\partial N_y}{\partial y} + \frac{\partial N_{xy}}{\partial x} + F_y = 0 \tag{2.12}$$

Finally, the plate equilibrium equation for the forces in z-direction is given by:

$$\frac{\partial Q_x}{\partial x} + \frac{\partial Q_y}{\partial y} = -F_z \tag{2.13}$$

The above three equations constitute the governing equations of a plate element in the translational degrees of freedom.

2.2.2 Moment equilibrium equations

After the force equilibria, we want to repeat the same process to obtain the moment equilibrium equations. Therefore we introduce Figure 2.4 showing the free body diagram of an infinitesimal IPMC plate element subjected to internal moments $\mathbf{M}$ about the in-plane axes.

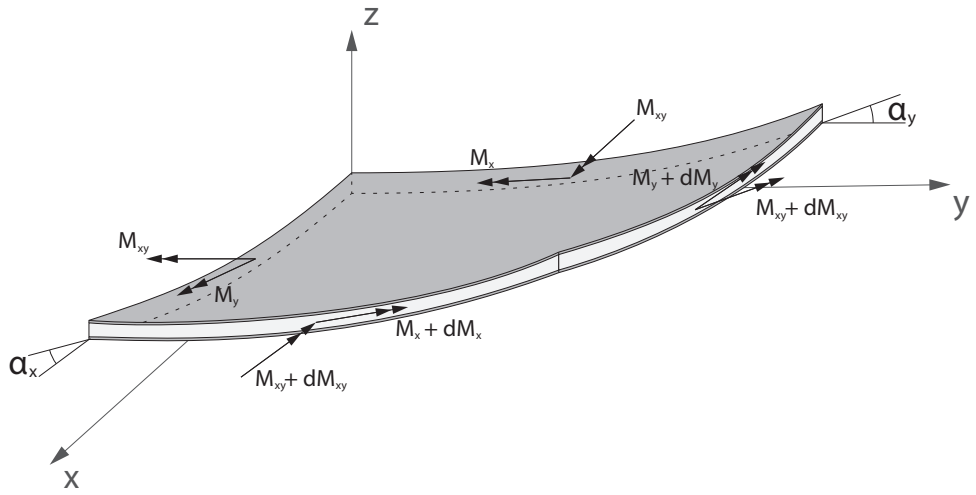

Figure 2.4: An infinitesimal IPMC plate element with deflection angles α_x and α_y and its internal moments $\mathbf{M}$. Adapted from: [10]

The complete derivation of the moment equilibrium equations, starting from the free body diagram up to the differential equations, can be found in Appendix A. Only the resulting differential equations are given in the remainder of this chapter.

From the moment equilibrium in x-direction, the equilibrium equation for moments about the x-axis is found to be:

$$\frac{\partial M_{xy}}{\partial x} + \frac{\partial M_x}{\partial y} = 0 \tag{2.14}$$

Similarly, the moments equilibrium about the y-axis produces an equilibrium equation given by:

$$\frac{\partial M_y}{\partial x} + \frac{\partial M_{xy}}{\partial y} = 0 \tag{2.15}$$

2.2.3 Electromechanical coupling

With the separate electric and mechanical behaviours of IPMC now discussed, we will have to fins a way to bring the two together in order to incite electroemchanical coupling. To add electromechanical deformation to the IPMC model we will add charge q as a term to the force and moment equilibrium equations. In this way, the charge will do its work from within the material itself, affecting the internal normal forces $\mathbf{N}$, shear forces $\mathbf{Q}$ and moments $\mathbf{M}$ of the plate.
Before we add the charge term, we find the definition of these forces and moments, shown in Figures 2.3 and 2.4, from the Classical Lamination Theory [1] as:

$$\mathbf{N} = \mathbf{A}\epsilon^0 + \mathbf{B}\kappa \tag{2.16}$$

$$\mathbf{Q} = \bar{\mathbf{Q}}\gamma \tag{2.17}$$

$$\mathbf{M} = \mathbf{B}\epsilon^0 + \mathbf{D}\kappa \tag{2.18}$$

where $\epsilon^{\mathbf{0}}$ is the in-plane strain on the bending neutral plane of the plate element, κ is the plate curvature and γ is the out-of-plane shear strain. Matrices $\mathbf{A}$, $\mathbf{B}$ and $\bar{\mathbf{Q}}$ are material properties of the composite plate.
With these expressions we are able to describe non-isotropic materials stacked into a composite material. With these equations, it is worth noting that matrix $\mathbf{B}$ contains only zeros for isotropic laminates [1] such as an ideal IPMC plate.

Now to apply the charge into these equations as per the modelling strategy [11]. Since we want it to induce only bending, and not normal or shear strains, we include it only as a factor in the definition of plate curvature κ. This extra, charge dependent term will induce curvature by adding to the internal normal forces $\mathbf{N}$ and internal moments $\mathbf{M}$ through Equations 2.16 and 2.18 respectively. Curvature is then defined as:

$$\kappa_x = \frac{\partial \alpha_x}{\partial x} + k_1 q, \qquad \kappa_y = \frac{\partial \alpha_y}{\partial y} + k_2 q, \qquad \kappa_{xy} = \frac{\partial \alpha_x}{\partial y} + \frac{\partial \alpha_y}{\partial x} \tag{2.19}$$

where, for the benefit of progress, we assume k_1 and k_2 to be some constants during the rest of this work. Note that by making this assumption, the model cannot account for back-relaxation of the actuator. Since the back-relaxation does significantly impact IPMC bending behaviour, it might be worthwhile in the future to introduce time dependence to these factors.

The definitions of the strain vectors $\epsilon^{\mathbf{0}}$ and γ remain as they are in the non-electromechanical case. Their definitions are given by:

$$\varepsilon_x^0 = \frac{\partial u}{\partial x}, \qquad \varepsilon_y^0 = \frac{\partial v}{\partial y}, \qquad \varepsilon_{xy}^0 = \frac{\partial u}{\partial y} + \frac{\partial v}{\partial x} \tag{2.20}$$

$$\gamma_{xz} = \frac{\partial w}{\partial x} + \alpha_x, \qquad \gamma_{yz} = \frac{\partial w}{\partial y} + \alpha_y \tag{2.21}$$

3 IPMC in FEM

Having obtained all of the required IPMC modelling equations in the previous section, it is time to implement them into a Finite Element scheme. For the sake of convenience, an existing FEM framework is taken wherein the new governing equations will be implemented through a dedicated IPMC element. The chosen framework is an open-source Python code called PyFEM[3]. This code was already capable of modelling standard plate elements with much of the same governing equations as derived in Chapter 2.2 with the exception of electromechanical coupling, of course.

In order to implement the IPMC specific equations a dedicated element type with electric and mechanical degrees of freedom is added to the framework.
In order to implement its governing equations, they have to be converted into matrix-vector format such that they can be solved numerically [15]. That means they have to be written in the form of:

$$\mathbf{K}\mathbf{a} = \mathbf{f} \tag{3.1}$$

where $\mathbf{K}$ is called the stiffness matrix, $\mathbf{a}$ is the vector containing the solutions to all degrees of freedom and $\mathbf{f}$ is the vector containing all the forces, both internal and external.
For a single node, vector $\mathbf{a}$ is defined as:

$$\mathbf{a} = \begin{bmatrix} p & u & v & w & r_x & r_y \end{bmatrix}^T \tag{3.2}$$

where p is the potential difference over the electrodes of the IPMC and u, v, w, r_x and r_y are the displacements in x-, y-, and z-direction and the curvatures in x- and y-direction, respectively.

In the remainder of this chapter, we will derive stiffness matrix $\mathbf{K}$ as well as the internal forces in vector $\mathbf{f}$ piece-by-piece. First we derive the contributions of the electric governing equation to each in Chapter 3.1. Secondly, we derive an equation to calculate the charge from potential distribution p in Chapter 3.2 Then, each of the mechanical contributions to the stiffness matrix and internal forces is calculated in Chapter 3.3.
Lastly, all of the obtained components are reassembled into the single matrix-vector system of equations of Equation 3.1 in Chapter 3.5.

3.1 Electric stiffness matrix

We begin the process of obtaining the components of the total stiffness matrix with the electric behaviour of IPMCs, taking the complete partial differential equation, in strong formulation, as given in Equation 2.1. After some rewriting, this becomes:

$$\frac{\partial}{\partial t}\left(\nabla \cdot \nabla \mathbf{p}\right) + \nabla \cdot \left(\frac{W}{C}\nabla \mathbf{p}\right) - \frac{\partial}{\partial t}\left(R\left(G+W\right)\mathbf{p}\right) - \frac{RGW}{C}\mathbf{p} = 0 \tag{3.3}$$

In order to solve this differential equation later on, we require it to be put into weak formulation first and then to be discretised in both space and time [16].
The weak form of the differential equation is obtained by integrating every term over the domain in which we work (Ω) and multiplying each with a so-called test function (ν) which we will define later on [18]. The weak form of the electric governing equation is:

$$\int_\Omega \frac{\partial}{\partial t}\left(\nabla \cdot \nabla \mathbf{p}\right)\nu \, d\Omega + \int_\Omega \nabla \cdot \left(\frac{W}{C}\nabla \mathbf{p}\right)\nu \, d\Omega - \int_\Omega \frac{\partial}{\partial t}\left(R\left(G+W\right)\mathbf{p}\right)\nu \, d\Omega - \int_\Omega \frac{RGW}{C}\mathbf{p}\nu \, d\Omega = 0 \tag{3.4}$$

Next, we would like to include the test function inside the brackets on the second derivative terms. This will aide in reducing the order of these derivatives. Moving the test function can be accomplished using the product rule for differentiation as:

$$(\nabla \cdot \nabla \mathbf{p})\,\nu = \nabla \cdot (\nabla \mathbf{p} \nu) - \nabla \nu \cdot \nabla \mathbf{p} \tag{3.5}$$

By substituting the right hand side terms of Equation 3.5 into the weak formulation of the PDE, we obtain:

$$\begin{aligned}\frac{\partial}{\partial t}\int_\Omega \nabla \cdot (\nabla \mathbf{p} \nu)\, d\Omega - \frac{\partial}{\partial t}\int_\Omega \nabla \nu \cdot \nabla \mathbf{p}\, d\Omega \\ + \int_\Omega \nabla \cdot \left(\frac{W}{C}\nabla \mathbf{p} \nu\right) d\Omega - \int_\Omega \nabla \nu \cdot \frac{W}{C}\nabla \mathbf{p}\, d\Omega \\ - \frac{\partial}{\partial t}\int_\Omega R\,(G+W)\,\mathbf{p}\nu\, d\Omega - \int_\Omega \frac{RGW}{C}\mathbf{p}\nu\, d\Omega = 0\end{aligned} \tag{3.6}$$

Now that the test functions are neatly inside the brackets in the second derivative terms, we can apply Gauss' divergence theorem, given by:

$$\int_\Omega \nabla \cdot \mathbf{a}\, d\Omega = \int_\Gamma \mathbf{a} \cdot \vec{n}\, d\Gamma \tag{3.7}$$

Applying Gauss' theorem on Equation 3.6 yields:

$$\begin{aligned}\frac{\partial}{\partial t}\int_\Gamma \nu \nabla \mathbf{p} \cdot \vec{n}\, d\Gamma - \frac{\partial}{\partial t}\int_\Omega \nabla \nu \cdot \nabla \mathbf{p}\, d\Omega \\ + \int_\Gamma \nu \frac{W}{C}\nabla \mathbf{p} \cdot \vec{n}\, d\Gamma - \int_\Omega \nabla \nu \cdot \frac{W}{C}\nabla \mathbf{p}\, d\Omega \\ - \frac{\partial}{\partial t}\int_\Omega R\,(G+W)\,\mathbf{p}\nu\, d\Omega - \int_\Omega \frac{RGW}{C}\mathbf{p}\nu\, d\Omega = 0\end{aligned} \tag{3.8}$$

which no longer contains any second order derivative.

The boundary integrals in Equation 3.8 are subject to the boundary conditions of the problem. The PyFEM framework contains a separate routine which enforces the boundary conditions after the system of equations has been solved. This allows us to omit the boundary integrals from this equation, which then simplifies to:

$$\begin{aligned}\frac{\partial}{\partial t}\int_\Omega \nabla \nu \cdot \nabla \mathbf{p}\, d\Omega + \int_\Omega \nabla \nu \cdot \frac{W}{C}\nabla \mathbf{p}\, d\Omega \\ + \frac{\partial}{\partial t}\int_\Omega R\,(G+W)\,\mathbf{p}\nu\, d\Omega + \int_\Omega \frac{RGW}{C}\mathbf{p}\nu\, d\Omega = 0\end{aligned} \tag{3.9}$$

Next, we use the Galerkin method to approximate the potential field p as a linear combination of expansion functions. We do this by discretising the potential field into n elements and multiply the potential difference over each element with their respective shape function φ. Furthermore we separate the variables of p, time and space, while doing so. This yields:

$$\mathbf{p}(\vec{x}, t) = \sum_{j=0}^{n} \mathbf{p}_j(t)\varphi_j(\vec{x}) \tag{3.10}$$

Next we substitute Equation 3.10 into Equation 3.9. At the same time we choose the test functions ν such that they correspond to the element shape functions φ to obtain:

$$\sum_{j=1}^{n} \frac{\partial \mathbf{p}_j}{\partial t} \left(\int_\Omega \nabla\varphi_i \cdot \nabla\varphi_j \, d\Omega + R\,(G+W) \int_\Omega \varphi_i \times \varphi_j \, d\Omega \right) + \sum_{j=1}^{n} \mathbf{p}_j \left(+ \frac{W}{C} \int_\Omega \nabla\varphi_i \cdot \nabla\varphi_j \, d\Omega + \frac{RGW}{C} \int_\Omega \varphi_j \times \varphi_i \, d\Omega \right) = 0 \quad (3.11)$$

All that stands in the way to solve this system of equations is the time derivative in the first term on the left-hand side. This derivative, approximated by an explicit Euler scheme, becomes:

$$\frac{\partial \mathbf{p}_j}{\partial t}^{k+1} = \frac{\mathbf{p}_j^{k+1} - \mathbf{p}_j^k}{\Delta t} \quad (3.12)$$

where k represents the current time step, for which the potential field is known, and $k+1$ represents the next time step to be solved. Then, by definition:

$$\mathbf{p}_j^{k+1} - \mathbf{p}_j^k = \Delta \mathbf{p}_j^{k+1} \quad (3.13)$$

We substitute these two expressions into Equation 3.11 to obtain:

$$\sum_{j=1}^{n} \Delta\mathbf{p}_j^{k+1} \left[\frac{1}{\Delta t} \left(\int_\Omega \nabla\varphi_i \cdot \nabla\varphi_j \, d\Omega + R\,(G+W) \int_\Omega \varphi_i \times \varphi_j \, d\Omega \right) + \left(\frac{W}{C} \int_\Omega \nabla\varphi_i \cdot \nabla\varphi_j \, d\Omega + \frac{RGW}{C} \int_\Omega \varphi_j \times \varphi_i \, d\Omega \right) \right] = - \sum_{j=1}^{n} \mathbf{p}_j^k \left(\frac{W}{C} \int_\Omega \nabla\varphi_i \cdot \nabla\varphi_j \, d\Omega + \frac{RGW}{C} \int_\Omega \varphi_j \times \varphi_i \, d\Omega \right) \quad (3.14)$$

We now have a system of n linear equations with n unknowns. It can be written in matrix-vector notation as:

$$\Delta p^{k+1} \cdot \left(\mathbf{K_{pp}} + \frac{\mathbf{C_{pp}}}{\Delta t} \right) = \mathbf{f_{p,int}} \cdot \mathbf{p}^k \quad (3.15)$$

where $\mathbf{K_{pp}}$ and $\mathbf{C_{pp}}$ are the stationary and instationary contributions to stiffness matrix from Equation 2.1 and $\mathbf{f_{p,int}}$ is the contribution to the internal forces vector from that same equation. They are defined as:

$$K_{pp|_{i,j}} = \frac{W}{C} \int_\Omega \nabla\varphi_i \cdot \nabla\varphi_j \, d\Omega + \frac{RGW}{C} \int_\Omega \varphi_i \times \varphi_j \, d\Omega \quad (3.16)$$

$$C_{pp|_{i,j}} = \int_\Omega \nabla\varphi_i \cdot \nabla\varphi_j d\Omega + R(G+W) \int_\Omega \varphi_i \times \varphi_j d\Omega \quad (3.17)$$

$$f_{p,int|_i} = -\frac{W}{C} \int_\Omega \nabla\varphi_i \cdot \nabla\varphi_j \, d\Omega - \frac{RGW}{C} \int_\Omega \varphi_i \times \varphi_j \, d\Omega \quad (3.18)$$

3.2 From potential to charge

Now that we are able to obtain the potential difference over the actuator, we need to obtain a numerically solvable expression of Equation 2.10. This could be achieved similarly to the PDE for potential. This is rather complex, however, for such a simple equation. Instead, it can be solved more easily by approximating the time derivative with an explicit Euler scheme. This yields:

$$\frac{d\mathbf{q}^{k+1}}{dt} = \frac{\mathbf{q}^{k+1} - \mathbf{q}^k}{\Delta t} \quad (3.19)$$

After substituting this expression into the differential equation for charge, we get:

$$C\frac{\mathbf{q}^{k+1}-\mathbf{q}^{k}}{\Delta t}+W\mathbf{q}^{k+1}=CW\mathbf{p}^{k+1} \tag{3.20}$$

For which we can isolate $\mathbf{q}^{k+1}$ on the left-hand side. This results in an equation to directly calculate the charge in capacitor C, namely:

$$\mathbf{q}^{k+1}=C\frac{W\mathbf{p}^{k+1}\Delta t+\mathbf{q}^{k}}{C+W\Delta t} \tag{3.21}$$

3.3 Mechanical stiffness matrix

Having obtained an expression to solve for the charge throughout the IPMC, we can move on with the mechanical stiffness and force contributions with electromechanical coupling. There are five mechanical contributions to each; one by each of the Equations 2.11, 2.12, 2.13, 2.14 and 2.15. These will be the starting point of obtaining the mechanical contributions of stiffness matrix $\mathbf{K}$.

3.3.1 Force equilibria

Starting from the force equilibrium equations for normal forces, we first obtain the weak form of both of these equations. The complete derivations of these weak forms are shown in Appendix B.
The in-plane weak formulations, for x- and y-directions respectively, are given by:

$$\int_{\Omega}\frac{\partial\nu}{\partial x}N_x d\Omega+\int_{\Omega}\frac{\partial\nu}{\partial y}N_{xy}d\Omega=0 \tag{3.22}$$

$$\int_{\Omega}\frac{\partial\nu}{\partial y}N_y d\Omega+\int_{\Omega}\frac{\partial\nu}{\partial x}N_{xy}d\Omega=0 \tag{3.23}$$

We obtain the components to force vector $\mathbf{N}$ from Equation 2.16. Writing out the individual expressions yields:

$$\begin{aligned}
N_x &= A_{11}\varepsilon_x^0+A_{12}\varepsilon_y^0+A_{16}\varepsilon_{xy}^0+B_{11}\kappa_x+B_{12}\kappa_y+B_{16}\kappa_{xy}\\
N_y &= A_{12}\varepsilon_x^0+A_{22}\varepsilon_y^0+A_{26}\varepsilon_{xy}^0+B_{12}\kappa_x+B_{22}\kappa_y+B_{26}\kappa_{xy}\\
N_{xy} &= A_{16}\varepsilon_x^0+A_{26}\varepsilon_y^0+A_{66}\varepsilon_{xy}^0+B_{16}\kappa_x+B_{26}\kappa_y+B_{66}\kappa_{xy}
\end{aligned} \tag{3.24}$$

After we plug Equations 2.19 and 2.20 into Equation 3.24, we can expand Equation 3.22 to obtain its contribution to the mechanical stiffness matrix. This is given by:

$$\begin{aligned}
K_{uu,u|_{i,j}}=\sum_{j=0}^{n}\int_{\Omega}\frac{\partial\varphi_i}{\partial x}&\left(\begin{bmatrix}A_{11}\\A_{16}\\0\\B_{11}\\B_{16}\end{bmatrix}^T\frac{\partial\varphi_j}{\partial x}+\begin{bmatrix}A_{16}\\A_{12}\\0\\B_{16}\\B_{12}\end{bmatrix}^T\frac{\partial\varphi_j}{\partial y}\right)+\\
&\frac{\partial\varphi_i}{\partial y}\left(\begin{bmatrix}A_{16}\\A_{66}\\0\\B_{16}\\B_{66}\end{bmatrix}^T\frac{\partial\varphi_j}{\partial x}+\begin{bmatrix}A_{66}\\A_{26}\\0\\B_{66}\\B_{26}\end{bmatrix}^T\frac{\partial\varphi_j}{\partial y}\right)d\Omega
\end{aligned} \tag{3.25}$$

The same expansion of Equation 3.23 leads to its own contribution to the mechanical stiffness matrix as:

$$K_{uu,v|_{i,j}} = \sum_{j=0}^{n} \int_{\Omega} \frac{\partial \varphi_i}{\partial y} \left(\begin{bmatrix} A_{12} \\ A_{26} \\ 0 \\ B_{12} \\ B_{26} \end{bmatrix}^T \frac{\partial \varphi_j}{\partial x} + \begin{bmatrix} A_{26} \\ A_{22} \\ 0 \\ B_{26} \\ B_{22} \end{bmatrix}^T \frac{\partial \varphi_j}{\partial y} \right) + \frac{\partial \varphi_i}{\partial x} \left(\begin{bmatrix} A_{16} \\ A_{66} \\ 0 \\ B_{16} \\ B_{66} \end{bmatrix}^T \frac{\partial \varphi_j}{\partial x} + \begin{bmatrix} A_{66} \\ A_{26} \\ 0 \\ B_{66} \\ B_{26} \end{bmatrix}^T \frac{\partial \varphi_j}{\partial y} \right) d\Omega \tag{3.26}$$

Similarly, in order to obtain the component to the mechanical stiffness matrix provided by Equation 2.13, we first have to derive its weak formulation. This derivation is shown in Appendix B and leads to:

$$\int_{\Omega} \frac{\partial \nu}{\partial x} Q_x d\Omega + \int_{\Omega} \frac{\partial \nu}{\partial y} Q_y d\Omega = 0 \tag{3.27}$$

where shear forces Q_x and Q_y are defined by Equation 2.17 and can be written as:

$$\begin{aligned} Q_x &= Q_{44}\gamma_{xz} + Q_{45}\gamma_{yz} \\ Q_y &= Q_{45}\gamma_{xz} + Q_{55}\gamma_{yz} \end{aligned} \tag{3.28}$$

Then, after combining the above equations and plugging in the definition of the out-of-plane shear strains, we obtain the last force contribution to mechanical stiffness matrix $\mathbf{K}$ as:

$$K_{uu,w|_{i,j}} = \sum_{j=0}^{n} \int_{\Omega} \frac{\partial \varphi_i}{\partial x} \left(\begin{bmatrix} 0 \\ 0 \\ Q_{44} \\ 0 \\ 0 \end{bmatrix}^T \frac{\partial \varphi_j}{\partial x} + \begin{bmatrix} 0 \\ 0 \\ Q_{45} \\ 0 \\ 0 \end{bmatrix}^T \frac{\partial \varphi_j}{\partial y} + \begin{bmatrix} 0 \\ 0 \\ 0 \\ Q_{44} \\ Q_{45} \end{bmatrix}^T \varphi_j \right) + \frac{\partial \varphi_i}{\partial y} \left(\begin{bmatrix} 0 \\ 0 \\ Q_{45} \\ 0 \\ 0 \end{bmatrix}^T \frac{\partial \varphi_j}{\partial x} + \begin{bmatrix} 0 \\ 0 \\ Q_{55} \\ 0 \\ 0 \end{bmatrix}^T \frac{\partial \varphi_j}{\partial y} + \begin{bmatrix} 0 \\ 0 \\ 0 \\ Q_{45} \\ Q_{55} \end{bmatrix}^T \varphi_j \right) d\Omega \tag{3.29}$$

3.3.2 Moment equilibria

For the two moment contributions to the mechanical stiffness matrix we repeat much of the same process as for the force equilibria. First we convert Equations 2.14 and 2.15 to their weak formulations. These derivations are shown in Appendix B and result in:

$$\int_{\Omega} \frac{\partial \nu}{\partial x} M_x \, d\Omega + \int_{\Omega} \frac{\partial \nu}{\partial y} M_{xy} \, d\Omega = 0 \tag{3.30}$$

$$\int_{\Omega} \frac{\partial \nu}{\partial x} M_{xy} \, d\Omega + \int_{\Omega} \frac{\partial \nu}{\partial y} M_y \, d\Omega = 0 \tag{3.31}$$

From Equation 2.18 we write down the individual components of the moments and obtain:

$$\begin{aligned} M_x &= B_{11}\varepsilon_x^0 + B_{12}\varepsilon_y^0 + B_{16}\varepsilon_{xy}^0 + D_{11}\kappa_x + D_{12}\kappa_y + D_{16}\kappa_{xy} \\ M_y &= B_{12}\varepsilon_x^0 + B_{22}\varepsilon_y^0 + B_{26}\varepsilon_{xy}^0 + D_{12}\kappa_x + D_{22}\kappa_y + D_{26}\kappa_{xy} \\ M_{xy} &= B_{16}\varepsilon_x^0 + B_{26}\varepsilon_y^0 + B_{66}\varepsilon_{xy}^0 + D_{16}\kappa_x + D_{26}\kappa_y + D_{66}\kappa_{xy} \end{aligned} \tag{3.32}$$

These expressions, along with Equations 2.19 and **??** are plugged into the weak formulations of the moment governing equations and their contributions to the stiffness matrix are retrieved.
For the moments about the x-axis, this is:

$$K_{uu,r_x|_{i,j}} = \sum_{j=0}^{n} \int_\Omega \frac{\partial \varphi_i}{\partial x} \left(\begin{bmatrix} B_{11} \\ B_{16} \\ 0 \\ D_{11} \\ D_{16} \end{bmatrix}^T \frac{\partial \varphi_j}{\partial x} + \begin{bmatrix} B_{16} \\ B_{12} \\ 0 \\ D_{16} \\ D_{12} \end{bmatrix}^T \frac{\partial \varphi_j}{\partial y} \right) + \frac{\partial \varphi_i}{\partial y} \left(\begin{bmatrix} B_{16} \\ B_{66} \\ 0 \\ D_{16} \\ D_{66} \end{bmatrix}^T \frac{\partial \varphi_j}{\partial x} + \begin{bmatrix} B_{66} \\ B_{26} \\ 0 \\ D_{66} \\ D_{26} \end{bmatrix}^T \frac{\partial \varphi_j}{\partial y} \right) d\Omega \tag{3.33}$$

and for the moments about the y-axis, the contribution to the stiffness matrix is:

$$K_{uu,r_y|_{i,j}} = \sum_{j=0}^{n} \int_\Omega \frac{\partial \varphi_i}{\partial x} \left(\begin{bmatrix} B_{16} \\ B_{66} \\ 0 \\ D_{16} \\ D_{66} \end{bmatrix}^T \frac{\partial \varphi_j}{\partial x} + \begin{bmatrix} B_{66} \\ B_{26} \\ 0 \\ D_{66} \\ D_{26} \end{bmatrix}^T \frac{\partial \varphi_j}{\partial y} \right) + \frac{\partial \varphi_i}{\partial y} \left(\begin{bmatrix} B_{12} \\ B_{26} \\ 0 \\ D_{12} \\ D_{26} \end{bmatrix}^T \frac{\partial \varphi_j}{\partial x} + \begin{bmatrix} B_{26} \\ B_{22} \\ 0 \\ D_{26} \\ D_{22} \end{bmatrix}^T \frac{\partial \varphi_j}{\partial y} \right) d\Omega \tag{3.34}$$

3.4 Electromechanical coupling

With all of the components to the total stiffness matrix sorted, we have still not coupled the electrical and mechanical behaviour. In fact, compared to the non-electromechanical case, the mechanical contributions to the stiffness matrix are not any different. The cause of this is that in their derivation, all terms with a dependency on charge were systematically moved to the other side of the equation. This other side must therefore contain the electromechanical coupling of the system.

It turns out that moving these charge dependent terms to the other side of the equations has led to expressions that we can equate to the internal forces, a part of vector $\mathbf{f}$ in Equation 3.1. These internal forces then add to the solutions of the displacements and rotations in vector $\mathbf{a}$, causing the IPMC to deflect. Only at this point will the IPMC element differ from a standard, mechanical plate element. Thus without any applied electric load nor any charge in the material, the IPMC element simplifies to the standard plate element.

Otherwise, with charge q present, the internal force due to the force equilibrium in x-direction is given by:

$$f_{int,u|_i} = -q_i \int_\Omega \frac{\partial \varphi_i}{\partial x} \left(k_1 B_{11} + k_2 B_{12}\right) + \frac{\partial \varphi_i}{\partial y} \left(k_1 B_{16} + k_2 B_{26}\right) d\Omega \tag{3.35}$$

of which the complete derivation is found in Appendix B; as are the other internal force terms in this chapter.

Likewise, the internal force due to the charge in the IPMC originating from the force equilibrium in y-direction is given by:

$$f_{int,v|_i} = -kq_i \int_\Omega \frac{\partial \varphi_i}{\partial y} \left(k_1 B_{12} + k_2 B_{22}\right) + \frac{\partial \varphi_i}{\partial x} \left(k_1 B_{16} + k_2 B_{26}\right) d\Omega \tag{3.36}$$

Again, it is important to note that matrix $\mathbf{B}$ only contains zero values for IPMCs [1], which are, ideally, isotropic laminates. The normal force contributions to the force vector will therefore also be zero. This makes sense since a nonzero component would cause contraction or elongation of the element, which is not observed behaviour of IPMC.

Then, we remember that the out-of-plane, internal shear forces were not dependent on curvature and therefore neither on charge. This means that the shear force has no contribution to force vector $\mathbf{f}$, thus:

$$f_{int,w|_i} = 0 \tag{3.37}$$

Now for the contributions to the internal forces due to the moment equilibrium equations. For the moments about the x-axis, it is shown in Appendix B that the contribution is:

$$f_{int,r_x|_i} = -q_i \int_\Omega \frac{\partial \varphi_i}{\partial x} \left(k_1 D_{11} + k_2 D_{12}\right) + \frac{\partial \varphi_i}{\partial y} \left(k_1 D_{16} + k_2 D_{26}\right) d\Omega \tag{3.38}$$

And for the moments about the y-axis it is:

$$f_{int,r_y|_i} = -q_i \int_\Omega \frac{\partial \varphi_i}{\partial x} \left(k_1 D_{16} + k_2 D_{26}\right) + \frac{\partial \varphi_i}{\partial y} \left(k_1 D_{12} + k_2 D_{22}\right) d\Omega \tag{3.39}$$

Unlike matrix $\mathbf{B}$, matrix $\mathbf{D}$ does not consist only of zeros. However, values D_{16} and D_{26} are zero when both electrodes of the IPMC are equal in thickness [1]. Nevertheless, the internal force for rotations r_x and r_y will therefore be nonzero as long as one of the factors k_1, k_2 as well as the charge are nonzero. These nonzero force terms will induce rotation of the element nodes leading to curvature of the mesh.

3.5 Total system of equations

In the beginning of this chapter, we introduced a general matrix-vector system, namely Equation 3.1, that can be solved numerically and which should represent all governing equations selected in Chapter 2. In Chapters 3.1, 3.3 and 3.4 we obtained all individual contributions of the governing equations to that system of equations. Now, it is time to assemble the total stiffness matrix $\mathbf{K}$ and force vector $\mathbf{f}$.

To this end we first define the mechanical stiffness matrix, assembled from the components to all the plate equilibrium equations found in Chapter 3.3, as:

$$\mathbf{K_{uu}} = \begin{bmatrix} K_{uu,u|_{1,1}} & \cdots & K_{uu,u|_{1,n}} \\ K_{uu,v|_{1,1}} & \cdots & K_{uu,v|_{1,n}} \\ K_{uu,w|_{1,1}} & \cdots & K_{uu,w|_{1,n}} \\ K_{uu,r_x|_{1,1}} & \cdots & K_{uu,r_x|_{1,n}} \\ K_{uu,r_y|_{1,1}} & \cdots & K_{uu,r_y|_{1,n}} \\ \vdots & \ddots & \\ K_{uu,u|_{n,1}} & \cdots & K_{uu,u|_{n,n}} \\ \vdots & & \vdots \end{bmatrix} \tag{3.40}$$

and, similarly, the deformation vector as:

$$\mathbf{u} = \begin{bmatrix} u & v & w & r_x & r_y \end{bmatrix}^T \tag{3.41}$$

Then the final system of equations to solve in the FEM framework becomes:

$$\begin{bmatrix} \mathbf{K_{pp}} + \mathbf{C_{pp}}/\Delta t & \mathbf{0} \\ \mathbf{0} & \mathbf{K_{uu}} \end{bmatrix} \begin{bmatrix} \Delta \mathbf{p} \\ \Delta \mathbf{u} \end{bmatrix} = \begin{bmatrix} \mathbf{f}_{ext,p} - \mathbf{f}_{int,p} \\ \mathbf{f}_{ext,u} - \mathbf{f}_{int,u} \end{bmatrix} \tag{3.42}$$

where $\mathbf{f}_{int,u}$ denotes all mechanical internal force contributions and $\mathbf{f}_{ext}$ are the externally applied loads to the actuator.

It is worth noting that $\mathbf{f}_{int,u}$, and therewith the solution to the mechanical degrees of freedom, is dependent on $\mathbf{p}$. This requires the system of equations to be solved in a staggered manner. This means that for every time step, first the system of equations must be solved only for the potential field. Then, for the same time step, the system of equations can be solved for deformation.

4 Numerical Verification

In the previous chapters, we have selected a modelling method and worked out the necessary mathematics. Now that this has all been implemented into PyFEM, the FEM framework, it is time to check the results from simulations that we know the (approximate) solution to.
We start with an introduction to the geometry, constraints and standard parameters used for the verification simulations in Chapter 4.1.
The first check will be to see if the potential field solution near the boundary between etched and unetched elements is correct. This can be found in Chapter 4.2.
Then, a series of simulations will be performed for limit cases with respect to the electrical parameters, which should match the solutions in Chapter 2.1. The results of these simulations can be found in Chapter 4.3.
Thirdly, the mechanical governing equations are tested for a problem with a known solution, a cantilevered beam, in Chapter 4.4.
Having checked both electrical and mechanical problems separately, the electromechanical coupling is verified in Chapter 4.5.
Finally, we will verify that the solutions to the potential, charge and out-of-plane displacement converge with mesh refinements, in Chapter 4.6, and with time step reduction, in Chapter 4.7.
Additionally, a small study was performed on the geometrical instabilities that may occur with simulations using IPMC elements. These instabilities are only present in exceptional cases and are thus added to the Appendix in C

4.1 Geometry and constraints

For the announced verification simulations, a common geometry is constructed; a rectangular actuator of 40 mm wide by 75 mm long by 2 mm thick. A square hole with 10 mm long sides is cut all the way through; with its center point located halfway across its width and 30 mm away from the base. The last 25 mm of its length has had the electrodes of both top and bottom surfaces etched away.
Figure 4.1 shows the geometry schematically.

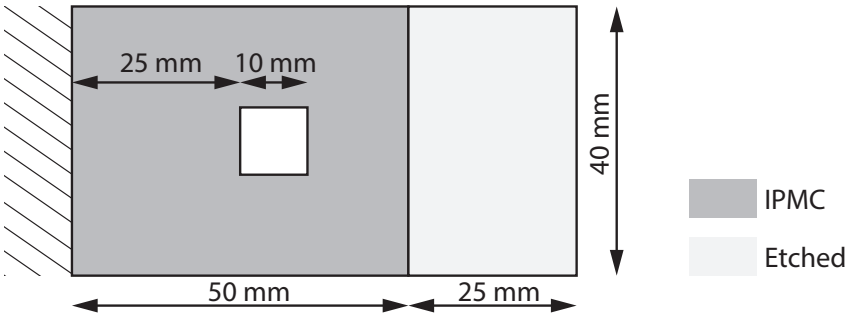

Figure 4.1: Schematic top-view representation of the actuator geometry used in the verification simulations

At the base the actuator is fully clamped as shown in the figure. All translational and rotational degrees of freedom at that edge are constrained to zero. The potential difference over the electrodes at the clamped base is constrained to 1 Volt.
Furthermore, unless otherwise specified, the relevant parameters used for all simulations in this chapter are:

Electrical			Mechanical			Other		
R	0.05	Ωmm^{-1}	E	1.00	MPa	Δt	0.10	s
C	0.03	$mFmm^{-1}$	ν	0.25		thickness	2.00	mm
W	0.04	$\Omega^{-1}mm^{-1}$	k_1	0.0				
G	0.007	$\Omega^{-1}mm^{-1}$	k_2	1.0				

Table 4.1: Standard simulation parameters for the verification simulations

The orders of magnitude for these numbers were taken from the paper by Vunder et al.[11]. Capacitance C and Conductivity W were moved closer together to obtain a resistor-capacitor time constant of less than 1 second. This time constant is a measure for the charging time of the capacitor. Reducing the time constant increases the rate at which the actuator responds and thus allows for the simulation of fewer time steps to model a fully bent actuator. This time constant is given by:

$$\tau = \frac{C}{W} \tag{4.1}$$

The value of conductivity G was increased by an order of magnitude in order to make its effect observable. Lastly, the surface resistance R was lowered in order to decrease the decay of potential difference over distance. This makes it that the actuator bends more evenly over its length instead of only at its base. This leads to more observable curvature.

4.2 Etched IPMC

The geometry of the previous section is first put to work in a simulation to confirm that the solution to the potential field around an etched boundary is correct. We run this simulation, with the geometry from Figure 4.1, and compare it to one where the square hole of that same geometry is replaced by etched material. If all is well, the solutions to the two simulations should be equal.

The solutions to the potential and charge were recorded over the length of the actuator on its centerline. Figure 4.2 shows the comparison between the solutions to the potential on the left and to the charge on the right.

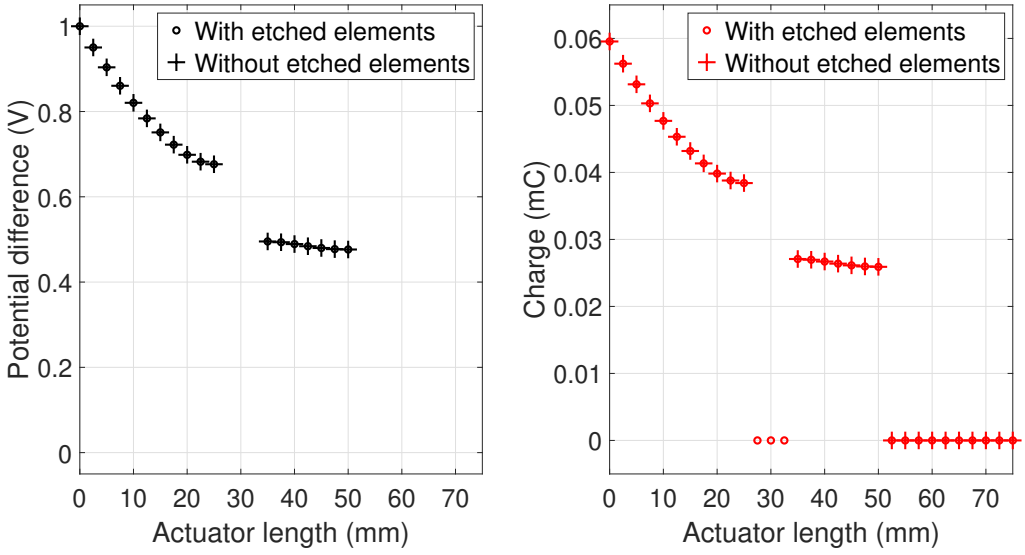

Figure 4.2: Potential difference and charge distributions for an IPMC actuator with a square hole and one with a square etching.

The figure shows that the solutions to the potential difference are perfectly equal. Even though there is etched material where the hole would normally be for one of the simulations, these etched elements do not conduct electricity and no solution to the potential difference is present. This explains the lack of data between 25-35 mm as well as the lack of data after 50 mm.
The difference in charge between the two simulations is equal as well. The three data points between 25-35 mm are from the etched elements that fill the square hole in the second simulation. Even though these elements do not conduct electricity, the solution vector for charge is initialised at 0 mC; thus a solution is still provided by the FEM framework. This same phenomenon explains the data points in the etched elements after 50 mm; which are present for both simulations.
As additional proof that the simulation results are equal, the root mean square error for both potential and charge was calculated. Both errors are exactly zero, from which we can conclude that etched geometries can be modelled without issue.

4.3 Qualitative analysis of the electric response

From testing the boundary between etched and IPMC elements, we move on to simulations of limit cases with respect to the electric parameters of the IPMC material. These simulations are set up to mimic the problems from Chapter 2.1.3.

In the first simulation test case, we eliminate the surface resistance of the IPMC ($R = 0\ \Omega mm^{-1}$) and observe that the entirety of the unetched part of the actuator instantly settles to 1V potential difference and remains as such indefinitely. According to the analytical solution from Chapter 4.3 this is correct.
Figure 4.3, made with Paraview, shows graphically the simulation result with the potential distribution on a color map. It shows a uniform potential difference over the IPMC material.

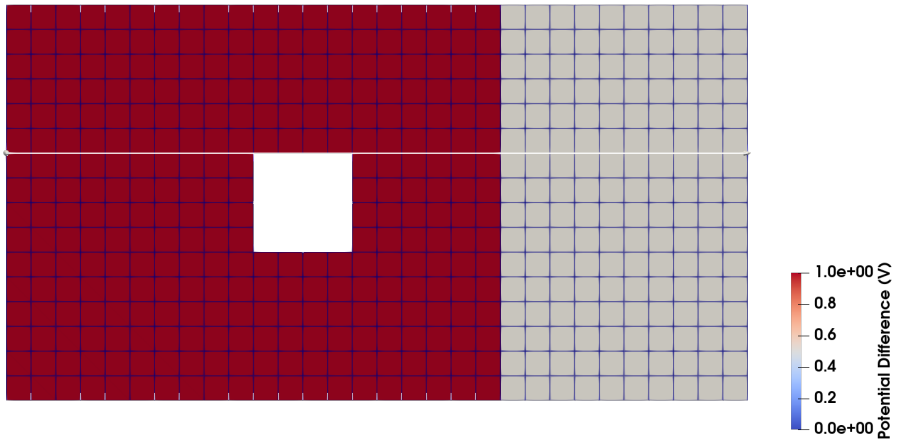

Figure 4.3: Potential difference distribution over an IPMC actuator for the limit case simulation with zero electric resistance in the electrodes.

To check the spatial dependence of the solutions, potential difference and charge data were collected over the length of the actuator and over the edge of the hole, visible in Figure 4.3 as a horizontal, white line.
Figure 4.4 shows the two solutions along that line for the simulations of all limit case problems.

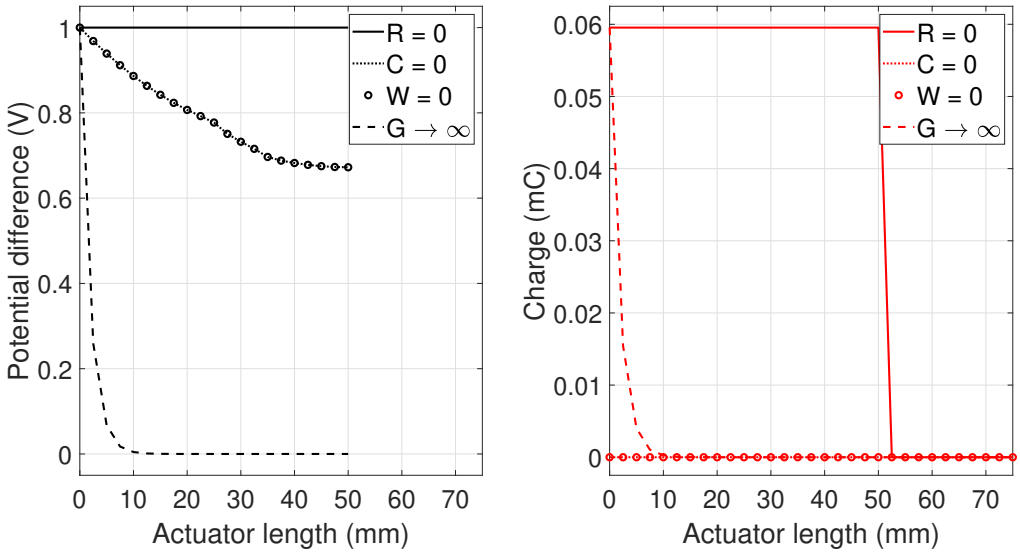

Figure 4.4: Electric response of an IPMC actuator, for four limit cases, to a 1V step signal (starting at $t = 0$s), graphed over its length.

It shows the uniform distribution of the potential difference, for the first limit case, and a uniform accumulation of charge due to this potential distribution. It matches the analytical solution in Chapter 2.1.3.

Secondly, to check the time dependence of the solutions, the potential and charge data are recorded over time on the top left corner of the square hole. Figure 4.5 shows the potential on the left and the charge on the right for the results of all limit case simulations.

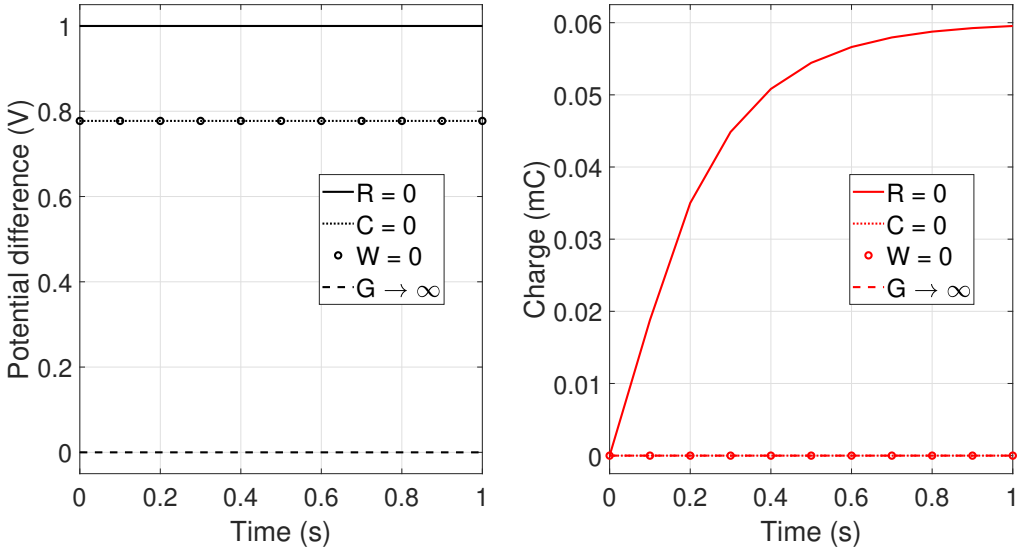

Figure 4.5: Electric response of an IPMC actuator, for four limit cases, to a 1V step signal (starting at $t = 0$s) of a single point on the actuator, graphed over time.

For the first limit case, it shows that the potential distribution is not dependent on time while the charge still is. This corresponds to the analytical solutions derived in Chapter 2.1.3. Furthermore, the charge curve shows that the capacitor is almost fully charged within one second. This is the result of the chosen values for the capacitance of C and the conductivity of W and their ratio as described by Equation 4.1.

Also note that the capacitance of the IPMC is equal to the capacitance of C multiplied with the thickness of the material.

For the second test case, we eliminate the capacitance of the IPMC ($C = 0\, mFmm^{-1}$) causing the capacitor not to conduct any electricity. We observe that the solution instantly settles to an exponentially decaying potential distribution over the length of the actuator. This is in agreement with the analytical solution in Chapter 4.3.
Figure 4.6 shows graphically the potential difference distribution over the unetched part of the actuator.

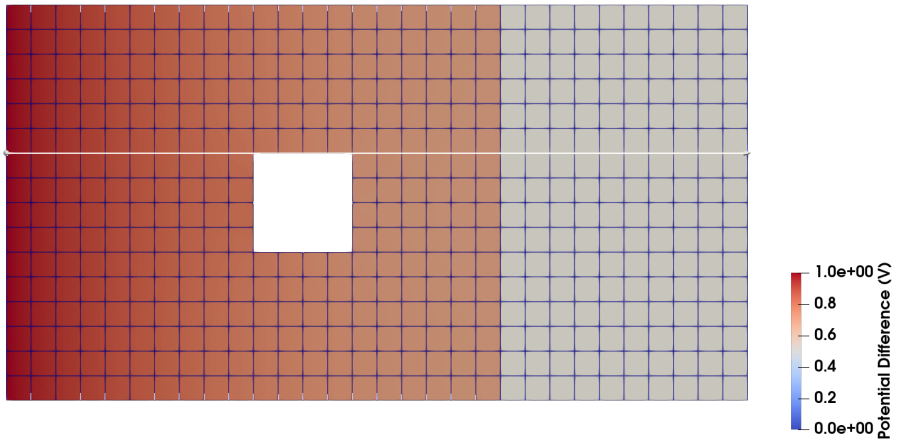

Figure 4.6: Potential difference distribution over an IPMC actuator for the limit case simulation with zero capacitance.

Figure 4.4 shows the potential difference and charge along the length of the actuator for the current limit case. The exponential potential difference decay shows a little kink at a distance of 25 mm away from the base. Not coincidentally, this is exactly where the square hole boundary starts. This hole causes the potential to 'pool up' near the blockage of current. Once past this blockage, the potential difference decays exponentially anew. The charge graph is zero everywhere, as expected for a capacitance of zero. Figure 4.5 shows their evolution over time. Since there is no capacitance, the potential distribution is independent of time and the charge remains zero. These results all correspond to the analytical solution in Chapter 2.1.3.

For the third test case we eliminate the conductivity through the capacitor ($W = 0\, \Omega^{-1}mm^{-1}$). This causes all current to bypass the capacitor preventing it from charging or discharging; similar to the second test case.
Figure 4.7 shows an equal potential distribution to that of the second test case, as was expected from the analytical solution in Chapter 2.1.3.

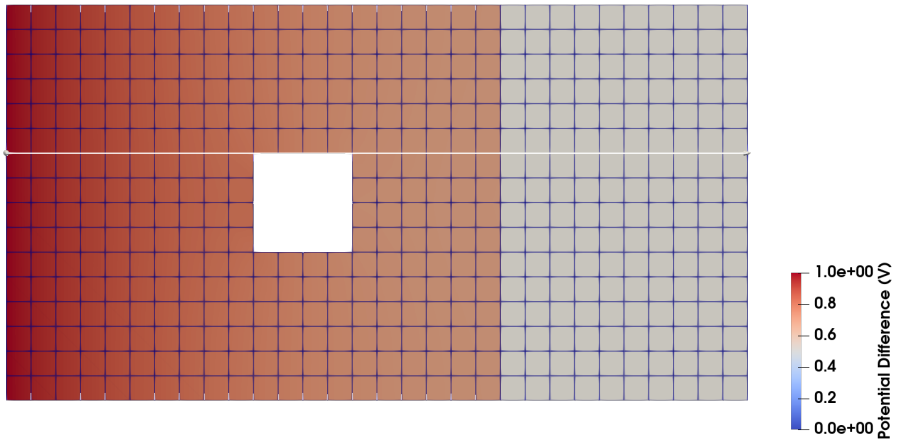

Figure 4.7: Potential difference distribution over an IPMC actuator for the limit case simulation with zero capacitive conductivity.

Figure 4.4 also shows that the potential distribution over the length of the actuator for this case is equal to the second case. The same is true for the distribution of charge. However this is equal to the previous case only because the initial state of charge of the actuator in this case was zero everywhere.
Figure 4.5 shows that the potential difference over time is stationary and that the charge in the material does not change over time.

For the final test case, we eliminate the resistance through the polymer ($G \rightarrow \infty\ \Omega^{-1}mm^{-1}$). For increasingly high values of conductance, the solution to the potential difference drops to zero quicker and quicker. At some value of conductance, the simulation becomes unstable, though, and the solution starts to oscillate. The chosen value for G is low enough not to cause significant oscillation.
Figure 4.8 graphically shows that the potential distribution over the actuator starts at 1V at the base and almost instantly drops to zero.

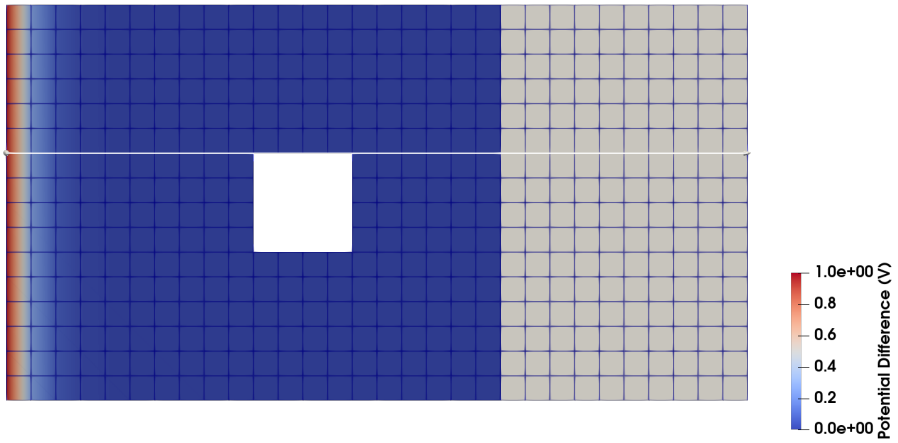

Figure 4.8: Potential difference distribution over an IPMC actuator for the limit case simulation where the electric conductivity of the polymer approaches infinity.

The potential difference and charge are shown over the length of the actuator in Figure 4.4. It tells the same story as the figure above; potential difference away from the constrained boundary is zero due to the approximate short-circuit of the material. Consequently, only close to the base of the actuator charge can accumulate since only here the potential difference can be nonzero.

Figure 4.5 shows that the top-left corner of the square hole is sufficiently far away from the base that a potential difference does not build up here. Because of that, charge also cannot accumulate; both remain zero.

4.4 Cantilevered plate

With the electric behaviour of the IPMC element checked in the previous chapter, it is time to make sure that the mechanical governing equations of the IPMC element are implemented correctly as well. To this end a simulation is set up without any applied electric potential. By doing this, we make sure that all results are obtained through the mechanical governing equations exclusively.
The simulation geometry consists of a long, slender, beamlike plate which is loaded by a distributed external force over the edge of the tip. The base of the plate is fully clamped and constrained to zero potential difference.
The relevant geometric and material parameters to this problem are given in Table 4.2. The simulations is performed with a mesh consisting of square elements 2.5 mm in size.

Property	Value	
F	-0.50	[N]
L	100	[mm]
b	10.0	[mm]
t	1.00	[mm]
E	1.00	[MPa]

Table 4.2: Geometric and material parameters to the clamped plate simulation with purely mechanical loads.

The simulation result of this problem is checked against the analytical solution to the tip deflection of a cantilevered beam. For the given geometry and constraints, the analytical solution to the deflection at the tip is given by:

$$w_{max} = \frac{FL^3}{3EI} \tag{4.2}$$

where the moment of inertia is:

$$I = \frac{bt^3}{12} \tag{4.3}$$

Then the deflection of the tip, as calculated by Equation 4.2, is -2.0 [mm]. The tip deflection as provided by the simulation with the IPMC element is -1.95 [mm]. This equates to a relative error of only 2.5%; therewith concluding that the IPMC elements are sufficiently accurate for mechanical loading.

4.5 Electromechanical deflection

We have confirmed that both electric and mechanical problems on their own are calculated correctly and provide good results. Now we need to check that the electromechanical coupling is working correctly as well.
For this problem, we take the cantilevered beam from the previous section, Chapter 4.4, and add a 1V potential difference constraint to the clamped base. Furthermore, we remove the external load at the tip and set surface resistance R to zero as this gives us a homogeneous charge distribution over the entire IPMC.
With a known and homogeneous charge in the IPMC we can manually calculate, from Equation 2.19, what the curvature must be. Additionally, from tip to base, the curvature must increase linearly at the rate of the magnitude of the charge per unit of length.

Figure 4.9 shows, in black, the rotation of the nodes of the cantilevered beam over its length. Due to the uniform charge distribution, each passed node adds an equal amount of rotation to the total, making it linear. The red markers represent the cumulative sum of the charge, multiplied with the element size, over the length of the actuator; starting from zero.

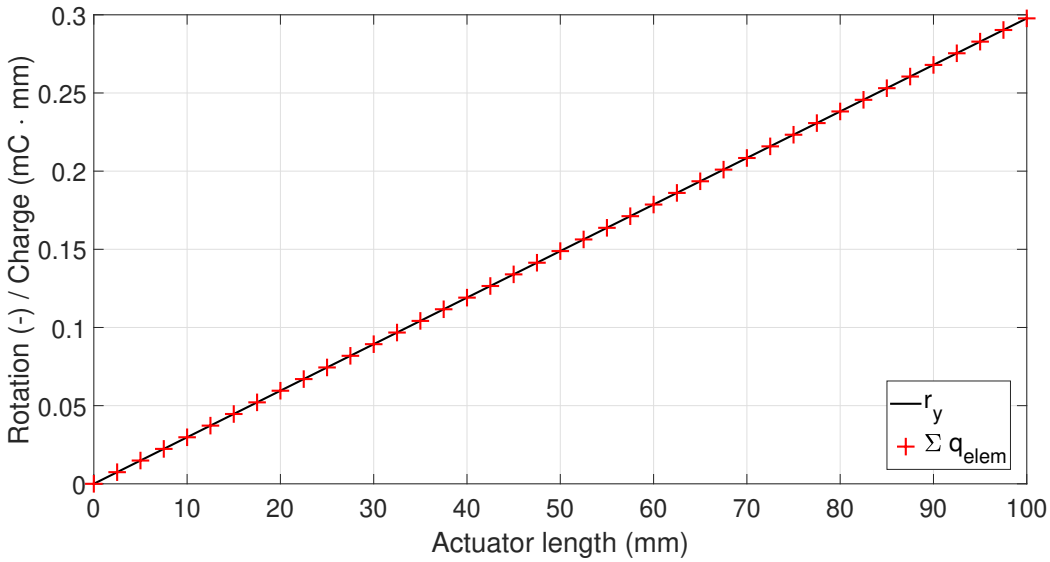

Figure 4.9: Cumulative sum of the charge, multiplied with the mesh element size, and rotation over the length of a non-etched, rectangular IPMC actuator without surface resistance.

From the figure it is apparent that the net amount of rotation of each node on the length of the actuator is equal to the cumulative sum of charge multiplied with the size of the corresponding element. This means that the added rotation with each node is equal to it charge multiplied with the element size.
This indicates that Equation 2.19 is implemented correctly. The electromechanical coupling thus works as intended.

4.6 Mesh convergence

Now that we have confirmed that the models for both electric and mechanical degrees of freedom have been implemented correctly and yield the expected results, it is time to check for convergence. First we will check that the solutions converge for reducing element sizes. To this end, four different meshes were made where the element size was halved at each step.
Figure 4.10 shows these meshes side-by-side from coarsest to finest. The absolute element size of each of these square-element meshes is given in Table 4.3.

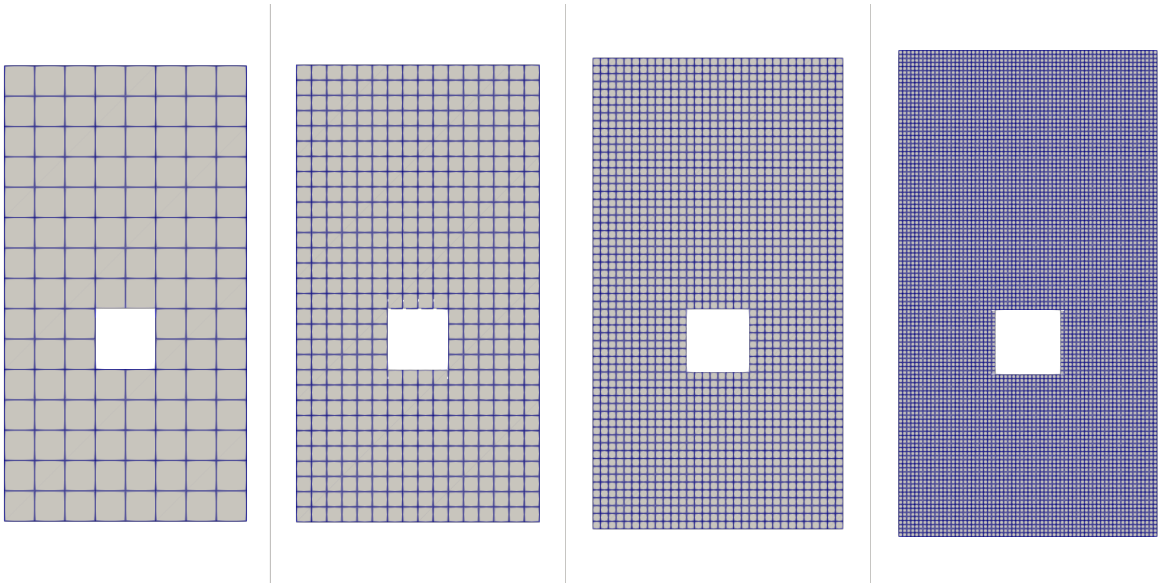

Figure 4.10: Meshes for the verification geometry, numbered #1 to #4 from coarsest to finest.

	Mesh #1	Mesh #2	Mesh #3	Mesh #4
Element size [mm]	5.00	2.50	1.25	0.625

Table 4.3: Absolute element sizes of all square-element meshes of the mesh convergence simulations.

Since there is no analytical solution on hand, convergence will be checked with respect to the solution of the finest mesh. The root mean square error of each simulation, to the results from the finest mesh, is shown in Table 4.4.

	RMSE w.r.t. Mesh #4		
Property	Mesh #1	Mesh #2	Mesh #3
p [V]	1.40E-3	5.39E-4	1.55E-4
q [mC]	2.22E-5	8.34E-6	2.40E-6
w [mm]	2.71E-4	7.78E-5	1.97E-5

Table 4.4: Root mean square error of the electric properties and out-of-plane displacement of IPMC nodes not on the boundaries.

The table shows that all solutions converge superlinearly for decreasing element size.

4.7 Time stepping convergence

The second check for convergence is with respect to time. Reducing the time step between subsequent cycles should result in more and more accurate results and the simulation results should show convergence. Simulations with time steps between 0.1 and 0.0001 seconds have been performed.
The chosen time intervals for the convergence simulations are given in Table 4.5.

	Δt_1	Δt_2	Δt_3	Δt_4	Δt_5
Time interval [s]	0.10	0.05	0.01	5E-3	1E-3

Table 4.5: Time stepping intervals of the mesh convergence simulations.

For these simulations we lack an analytical solution as well so convergence will be tested with respect to the simulation with the smallest time step. The root mean square of each simulation, to the results from the smallest time step, is shown in Table 4.6.

	RMSE w.r.t. Δt_5			
Property	Δt_1	Δt_2	Δt_3	Δt_4
p [V]	3.71E-3	1.86E-3	3.46E-4	1.54E-4
q [mC]	9.42E-4	4.62E-4	8.44E-5	3.75E-5
w [mm]	8.76E-4	4.31E-4	7.89E-5	3.50E-5

Table 4.6: Root mean square error of the electric properties of IPMC nodes not on the boundaries.

The table shows that all solutions converge superlinearly for decreasing time step.

5 Use Cases

Now that we have a working and tested FEM model for IPMC actuators, it is time to explore its capabilities. First up, in Chapter 5.1, is an example of a parameter study testing the electric response of a simple rectangular IPMC actuator to changes in the electrical parameters. Secondly, in Chapter 5.2, we model a monolithic actuation unit as introduced in Chapter 1 of this report. Finally, in Chapter 5.3, we compare an actuator with kirigami slicing patterns to one without and show that it significantly affects the deflection of the actuator.

5.1 Parameter study

In the first show of use cases, we perform a parameter study on the electric material properties of IPMCs. More specifically, we test the response in deflection when changing the electric material properties. Each of the components from the electric representative circuit R, C, G and W are subjected to a variation for this study.
The geometry used to perform the parameter study is the same rectangular IPMC actuator described in Chapter 4.4. The electric material properties are the same as in Table 4.2, unless otherwise specified. With these simulations, the clamped edge is constrained to a 1V potential difference instead of 0V and the mechanical load at the tip is removed.
Figure 5.1 shows the deflection over the length on the centerline of the actuator.

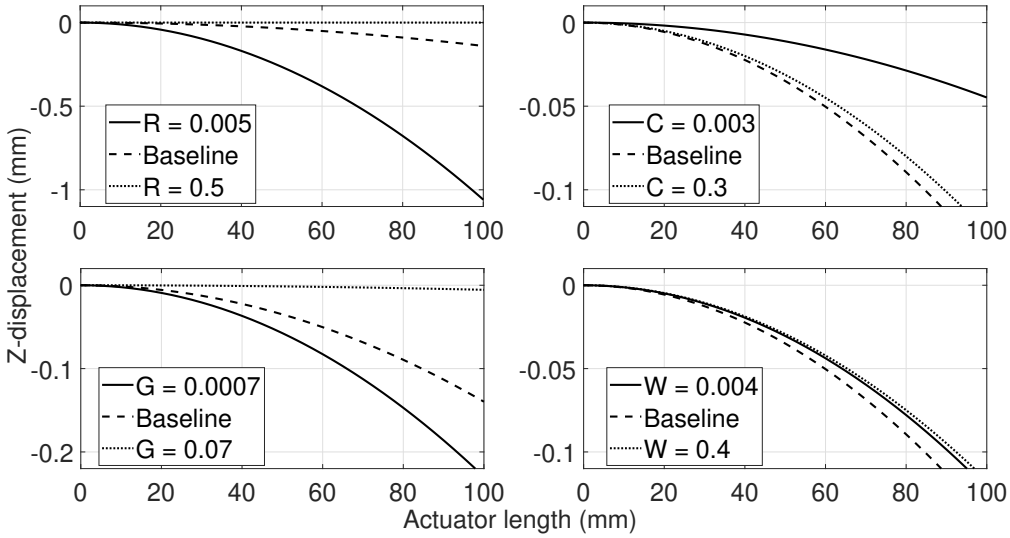

Figure 5.1: Deflection of a non-etched, rectangular IPMC actuator for varying electric material properties.

From the deflection results of the parameter variation for the surface resistance R, we see that every decrease in surface resistance leads to an increase in deflection. This may seem obvious, however, if we look at the deflection for increasing capacitance C we see that the final increase led to a decrease in deflection. This phenomenon occurs due to the fact that the capacitors near the base of the actuator conduct so much current that the later capacitors are unable to charge and therefore induce less curvature.
For reducing leakage conductivity G, we see again that the actuator deflects more with less leakage; which is to be expected.
The last parameter we look at is the capacitive conductivity W. Either increasing or decreasing it with respect to the baseline leads to less deflection of the actuator. This is intuitive for the case of less conductivity but for the case of more conductivity we once again run into the situation that much of the

current flows through the IPMC close to the base, hindering the curvature at locations further away.

With these results a sensitivity analysis can be done on the electric parameters. This could be used to optimise the use of materials in the composite. A similar analysis could be performed for the thickness of the polymer membrane or any other property.

5.2 Monolithic actuator with eight actuation units and no Kirigami

The second use case is one that showcases the capability of the IPMC element to be used to model monolithic actuators. This use case is an important one since the purpose of this work is to be able to calculate the electromechanical response of actuators such as these; comprised of multiple actuation units. A simulation was set up to specifically resemble the monolithic actuators that will be modeled with it in future research.

This monolithic actuator is designed with eight IPMC actuation units in a two-by-four array. The actuator is subdivided into four sets of opposing actuation units moving together. In order to decrease simulation time, only two actuation units are modelled explicitly. The rest of the geometry is implied with the use of constraints. The explicitly modelled units are the two middle units each of separate actuation pairs.
The edge on the symmetry plane is constrained to zero displacement and zero curvature in the in-plane direction, normal to the edge. These constraints serve to impose symmetry on the geometry.
The exposed sides besides the actuation units are constrained to zero displacement in the direction out-of-plane and in the direction in-plane, normal to the edge.
Lastly, the base of the actuator is fully clamped and the units are constrained to a ± 1V potential difference.
Figure 5.2 schematically shows the geometry and constraints of this problem. Note that the roller guides on the sides indicate that longitudinal displacements are permitted as well as all rotations.

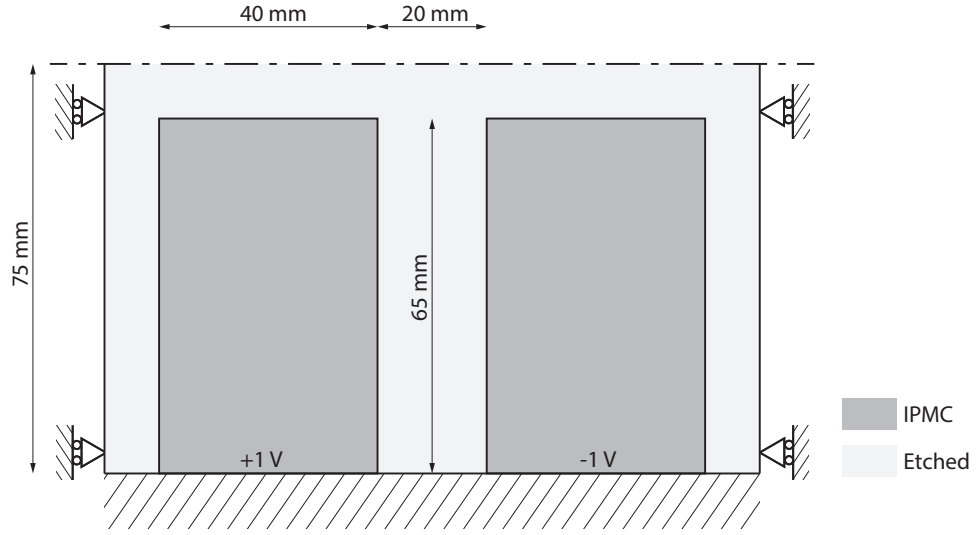

Figure 5.2: Schematic representation of a twin-actuation-unit IPMC actuator representative of an actuator comprised of eight units.

With this simulation, the free sides of the actuator are not modelled. If the behaviour at those locations is of interest, the geometry and constraints can be adapted to suit. The constraints as chosen not only represent an eight-unit actuator, but are valid for any twin row actuator with eight or more units.

The deformation that results from the mentioned simulation is shown in Figure 5.3. The colors are representative of the potential difference over the actuation units, where red means a positive and blue a negative voltage.

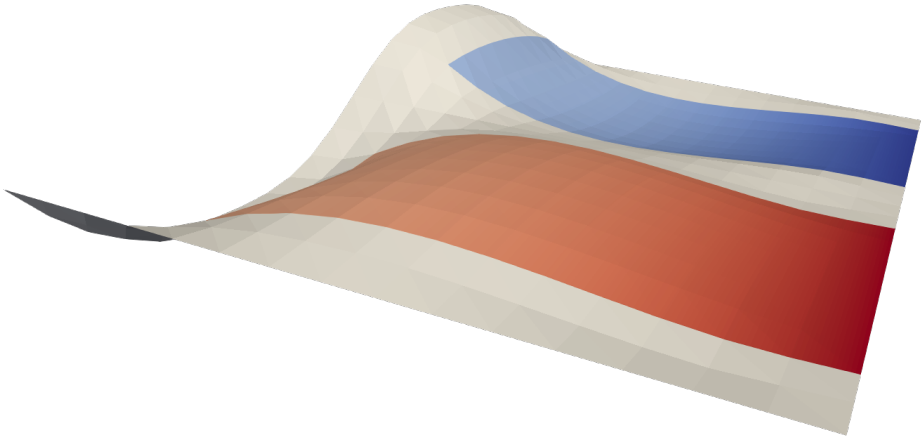

Figure 5.3: Three-dimensional representation of the displacement field of a simulated monolithic IPMC actuator with eight actuation units. Red indicates a positive voltage up to 1V, blue indicates a negative voltage down to -1V.

In order to promote displacement for better visualisation, the Young's modulus of the etched elements was reduced by 90% with respect to that of the IPMC. Furthermore, the displacement was scaled by a factor 3 for visualisation.

Figure 5.4 shows the stresses on the bottom of the etched parts of the actuator resulting from the deformation. Note that the cut-off corners in the IPMC actuation units is a flaw in the graphical representation of the solution and not an actual phenomenon.

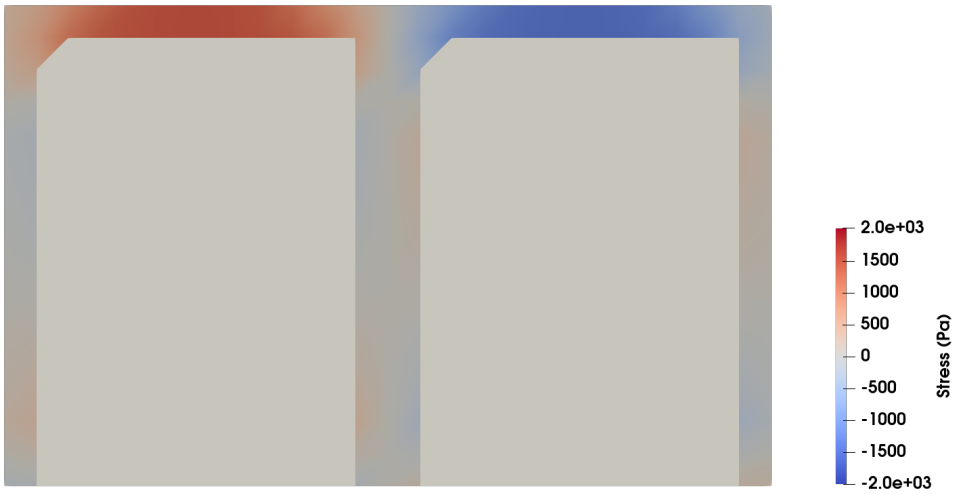

Figure 5.4: Stresses in the monolithic actuator with eight actuation units.

The figure shows that most of the stress in the etched part of the actuator is concentrated near the centers of the tips of the actuation units. Images like these could be used to identify regions where implementing

stress-relieving Kirigami cuts is most effective.

5.3 Monolithic actuator with two actuation units and Kirigami

Now that we know that the FEM model is able to simulate monolithic IPMC actuators, the next step is to add Kirigami patterns and compare the displacements to their non-Kirigami counterparts.
To this end, we propose a monolithic actuator comprised of only two actuation units moving together. The two units are placed opposite to each other and are electronically separated by an etched region in between. Only half of the actuator is modelled explicitly and constraints are added to enforce symmetry. At the plane of symmetry, the displacement of the edge is constrained in the out-of-plane direction and the direction in-plane, normal to the edge. Additionally, curvature in the direction normal to the edge is constrained to zero. The base of the actuator is fully clamped and constrained to 1V potential difference. The electric parameters of the simulation are given in Table 4.2 and the geometry is shown in Figure 5.5.

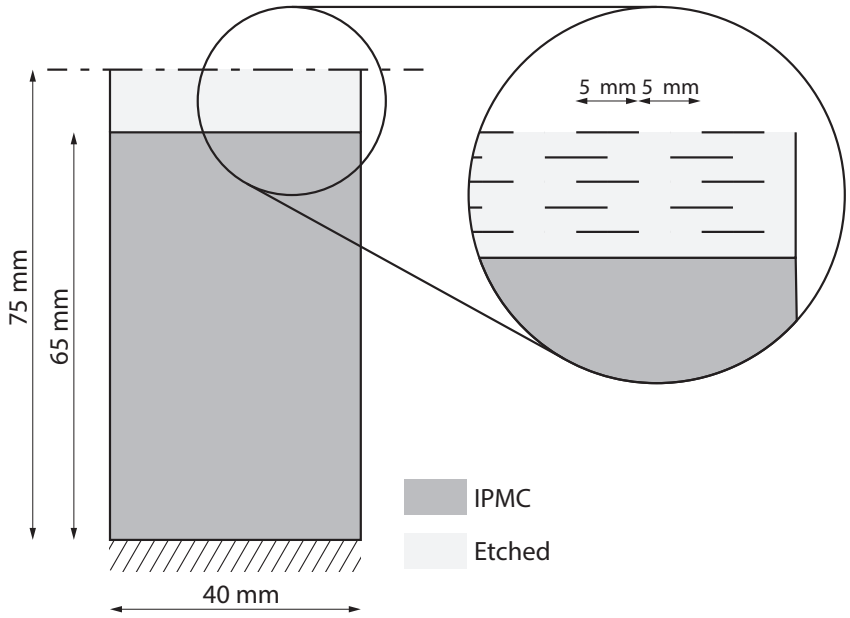

Figure 5.5: Schematic representation of one half of a monolithic IPMC actuator with two actuation units.

The first simulation with this geometry is executed without kirigami cutting patterns. The second simulation will include a cutting pattern on the etched part. The cuts are directed transversely to the actuator and rectangular in shape; 5 mm long by 1 mm wide. Head-to-tail the cuts are spaced 5 mm apart. The rows of Kirigami cuts are staggered and spaced 1 mm apart. The row closest to the actuation unit is 1.5 mm away from the tip of that unit.

Figure 5.6 shows the potential difference and displacement over the length of the actuator on the centerline at $t = 1.0$ s in black. It shows that for an identical potential distribution, the actuator with Kirigami cuts is able to deflect significantly more.

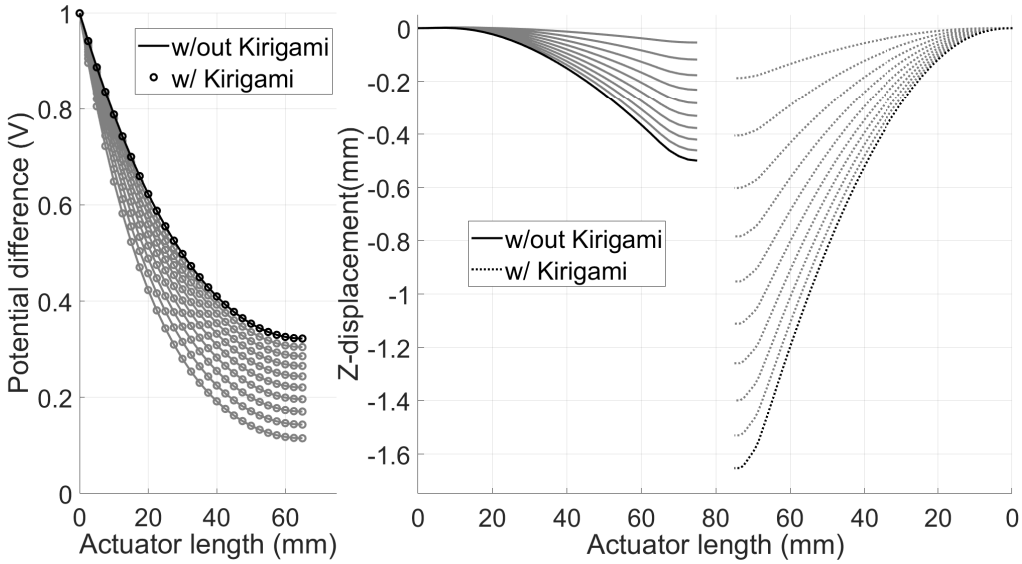

Figure 5.6: Potential difference and deflection at the centerline of IPMC actuators with and without Kirigami stress-relief cuts from $t = 0.1$ s to $t = 1.0$ s.

The grey lines in the figure indicate the potential distribution and deflection of the actuators from $t = 0.1$ s to $t = 0.9$ s in nine steps.
Results like these can be used to evaluate or compare the effectiveness of different Kirigami patterns in actuators.

Figure 5.7 shows a three dimensional view of the same two actuators from the same simulation in their deflected state at $t = 1.0$ s.

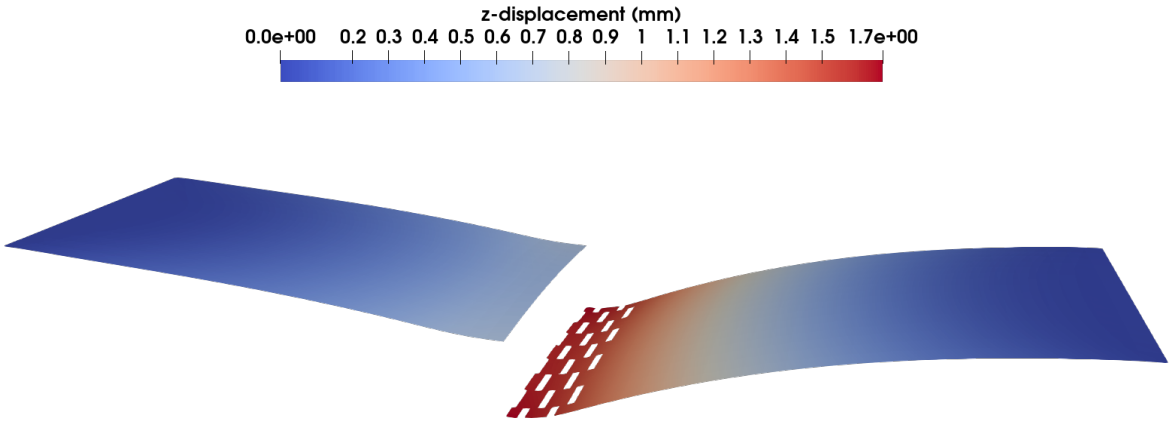

Figure 5.7: Three-dimensional representation of the displacement field of IPMC actuators with two actuation units, with and without Kirigami patterns.

With the increased deflection from Kirigami patterns comes reduced strength of the etched membrane. It is important to know at which point the slits have compromised the integrity of the actuator too much. Therefore, the stresses can be displayed over the geometry as shown in Figure 5.8.

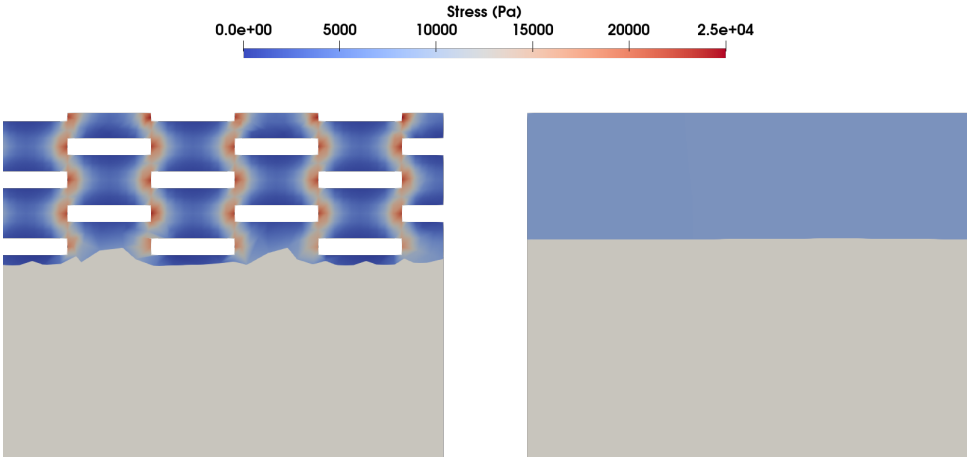

Figure 5.8: Close-up of the stresses in the etched regions of IPMC actuators with two actuation units, with and without kirigami patterns.

Note that the stresses in the first row of elements from the actuation unit into the etched part is not shown. This is caused by a flaw in the graphical representation of the solution and not an actual phenomenon.

6 Conclusion

IPMCs are a soft, smart, electromechanical composite material. Active research is done on its use as actuator in a linear peristaltic pump [17]. These monolithic actuators with multiple actuation units are manufactured from a single sheet of IPMC. The research focuses on the use of slit patterns in the actuator to increase performance. In aid of this research, we develop a numerical model, making it possible to perform numerical analyses on the complex geometries of actuators such as these.
To this end we have selected models from the literature to represent both the electric and mechanical behaviour of IPMC actuators. We then established a one-way electromechanical coupling by adding charge dependent terms to the mechanical model.
Subsequently, we converted the coupled models into a system of equations and integrated into PyFEM, a Python based FEM framework. The work was tested with simulations of problems with known solutions as numerical verification.

A fully functional IPMC-plate FEM element was developed which can be used in PyFEM. With it, it is possible to simulate complex IPMC actuator geometries such as monolithic actuators comprised of multiple actuation units.
Furthermore, it was shown that the use of slit patterns in IPMC actuator design significantly affects the performance of the actuator. The simulation outputs, such as deformation and stress, make extensive design analyses on such designs possible and allows the user to make qualitative predictions on the performance of IPMC actuators.

The following opportunities for further development of the FEM element may be worthwhile: Firstly, the simulations do not model the back-relaxation of strain; which is characteristic of IPMCs. In the future this could be implemented, for instance, by changing the coupling quantity from charge to its time derivative, current, since charge only accumulates for a step signal while current also recedes. Another option is to exchange constant coupling terms k_1 and k_2 with instationary ones.
Secondly, IPMCs cannot be modelled in sensor mode due to the one-way nature of the introduced electromechanical coupling; with deformation dependent on charge and not vice-versa. In order to model the sensor mode of IPMCs, an additional model could be introduced which makes the electric degree of freedom dependent on deformation.
Lastly, while it was verified numerically, the model was not validated empirically. We know that the model behaves as expected but not if it does so accurately in magnitude. This makes the model suited for qualitative studies on the design and material properties of actuators. However, for quantitative results, the modelling parameters need to be validated against experimental results.

Bibliography

[1] Charles W. Bert. "Section IIB Classical Lamination Theory". In: *Manual on Experimental Methods for Mechanical Testing of Composites*. Ed. by Richard L. Pendleton and Mark E. Tuttle. Dordrecht: Springer Netherlands, 1989, pp. 11–16. ISBN: 978-94-009-1129-1. DOI: 10.1007/978-94-009-1129-1_3. URL: https://doi.org/10.1007/978-94-009-1129-1_3.

[2] Jack R. Vinson. "Chapter 2 Derivation of the Governing Equations for Beams and Rectangular Plates". In: *The Behaviour of Thin Walled Structures*. Springer, 1989, pp. 9–23. ISBN: 978-94-009-2774-2. DOI: 10.1117/3.547465. URL: https://doi.org/10.1007/978-94-009-2774-2.

[3] D. Borst et al. "Non-Linear Finite Element Analysis of Solids and Structures". In: 1991.

[4] R. Kanno et al. "Linear approximate dynamic model of ICPF (ionic conducting polymer gel film) actuator". In: *Proceedings of IEEE International Conference on Robotics and Automation*. Vol. 1. 1996, 219–225 vol.1. DOI: 10.1109/ROBOT.1996.503781.

[5] S. Tadokoro et al. "An actuator model of ICPF for robotic applications on the basis of physicochemical hypotheses". In: *Proceedings 2000 ICRA. Millennium Conference. IEEE International Conference on Robotics and Automation. Symposia Proceedings (Cat. No.00CH37065)*. Vol. 2. 2000, 1340–1346 vol.2. DOI: 10.1109/ROBOT.2000.844784.

[6] Yoseph Bar-Cohen. "Chapter 1 EAP History, Current Status, and Infrastructure". In: *Electroactive Polymer (EAP) Actuators as Artificial Muscles: Reality, Potential, and Challenges*. SPIE, 2004, pp. 3–52. ISBN: 978-0-81948-112-2. DOI: 10.1117/3.547465. URL: https://doi.org/10.1117/3.547465.

[7] Satoshi Tadokoro and Masashi Konyo. "Chapter 13 Modeling IPMC for design of actuation mechanisms". In: *Electroactive Polymer (EAP) Actuators as Artificial Muscles: Reality, Potential, and Challenges*. SPIE, 2004, pp. 385–430. ISBN: 978-0-81948-112-2. DOI: 10.1117/3.547465. URL: https://doi.org/10.1117/3.547465.

[8] K. Farinholt. "Modeling and characterization of ionic polymer transducers for sensing and actuation". In: 2005.

[9] Zheng Chen, T. Um, and Hilary Bart-Smith. "Ionic Polymer-Metal Composite Artificial Muscles in Bio-Inspired Engineering Research: Underwater Propulsion". In: *Smart actuation and sensing systems - recent advances and future challenges*. Rijeka: InTech, Jan. 2012, pp. 223–248. ISBN: ISBN 978-953-51-0798-9.

[10] Joris J. C. Remmers. *Lecture notes on Plate Equilibrium Equations*. Mar. 2012.

[11] Veiko Vunder, Andres Punning, and Alvo Aabloo. "Mechanical interpretation of back-relaxation of ionic electroactive polymer actuators". In: *Smart Materials and Structures* 21.11 (Oct. 2012), p. 115023. DOI: 10.1088/0964-1726/21/11/115023. URL: https://doi.org/10.1088/0964-1726/21/11/115023.

[12] David Vokoun et al. "Modeling of IPMC Cantilever's Displacements and Blocking Forces". In: *Journal of Bionic Engineering* 12.1 (2015), pp. 142–151. ISSN: 1672-6529. DOI: https://doi.org/10.1016/S1672-6529(14)60108-6. URL: https://www.sciencedirect.com/science/article/pii/S1672652914601086.

[13] Mohsen Shahinpoor. "Chapter 1 Fundamentals of Ionic Polymer Metal Composites (IPMCs)". In: *Ionic Polymer Metal Composites (IPMCs): Smart Multi-Functional Materials and Artificial Muscles*. Vol. 1. The Royal Society of Chemistry, 2016, pp. 1–60. ISBN: 978-1-78262-077-8. DOI: 10.1039/9781782622581-00001. URL: http://dx.doi.org/10.1039/9781782622581-00001.

[14] Miguel A. López et al. “Frequency response of IPMC actuators: physical characterization and identification for control”. In: *Actas de las XXXIX Jornadas de Automática*. 2018, pp. 717–724. URL: https://doi.org/10.17979/spudc.9788497497565.0717.

[15] M. Okereke and S. Keates. “Direct Stiffness Method”. In: *Finite Element Applications: A Practical Guide to the FEM Process*. Cham: Springer International Publishing, 2018, pp. 47–106. ISBN: 978-3-319-67125-3. DOI: 10.1007/978-3-319-67125-3_3. URL: https://doi.org/10.1007/978-3-319-67125-3_3.

[16] M. Okereke and S. Keates. “Mathematics of Element Formulation”. In: *Finite Element Applications: A Practical Guide to the FEM Process*. Cham: Springer International Publishing, 2018, pp. 187–241. ISBN: 978-3-319-67125-3. DOI: 10.1007/978-3-319-67125-3_7. URL: https://doi.org/10.1007/978-3-319-67125-3_7.

[17] E. A. Sideris, H. C. de Lange, and A. Hunt. “An Ionic Polymer Metal Composite (IPMC)-Driven Linear Peristaltic Microfluidic Pump”. In: *IEEE Robotics and Automation Letters* 5.4 (2020), pp. 6788–6795. DOI: 10.1109/LRA.2020.3015452.

[18] J. M. Burgerscentrum and A. Segal. *Lecture notes on the Finite element methods for the incompressible Navier-Stokes equations*. 2021.

Declaration concerning the TU/e Code of Scientific Conduct for the Master's thesis

I have read the TU/e Code of Scientific Conduct[i].

I hereby declare that my Master's thesis has been carried out in accordance with the rules of the TU/e Code of Scientific Conduct

Date

07-04-2021

Name

H.A. de Reuver

ID-number

0892382

Signature

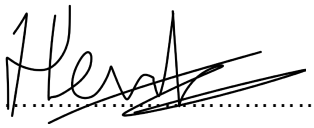

Submit the signed declaration to the student administration of your department.

[i] See: http://www.tue.nl/en/university/about-the-university/integrity/scientific-integrity/
The Netherlands Code of Conduct for Academic Practice of the VSNU can be found here also.
More information about scientific integrity is published on the websites of TU/e and VSNU

A Plate Equations

A.1 Force equilibrium equations

From the free-body diagram in Figure 2.3 it follows that the sum of forces in x-direction is given by:

$$(N_x + dN_x)\, dy \cos\alpha_x - (Q_x + dQ_x)\, dy \sin\alpha_x + (N_{xy} + dN_{xy})\, dx - N_{xy}dx - N_x dy + p_x dxdy = 0 \quad \text{(A.1)}$$

For an infinitesimal element we assume small deformation angles such that $\cos\alpha_x \approx 1$ and $\sin\alpha_x \approx \alpha_x$. We then substitute these into the equation above and divide every term by $dxdy$ to obtain:

$$\frac{\partial N_x}{\partial x} + \frac{\partial N_{xy}}{\partial y} - Q_x\frac{\alpha_x}{dx} - \frac{\partial Q_x}{\partial x}\alpha_x + p_x = 0 \quad \text{(A.2)}$$

In this equation, the plate deflection angles (α_x and α_y) can be expressed in terms of displacement in z-direction (w) according to:

$$\alpha_x = \frac{\partial w}{\partial x}, \qquad \alpha_y = \frac{\partial w}{\partial y} \quad \text{(A.3)}$$

Plugging these into Equation A.2 and omitting the higher order terms leads to Equation A.4.
Similarly, if we follow the same steps for the force equilibrium in y-direction, we obtain Equation A.5.

$$\frac{\partial N_x}{\partial x} + \frac{\partial N_{xy}}{\partial y} - Q_x\frac{\partial^2 w}{\partial x^2} + F_x = 0 \quad \text{(A.4)}$$

$$\frac{\partial N_y}{\partial y} + \frac{\partial N_{xy}}{\partial x} - Q_y\frac{\partial^2 w}{\partial y^2} + F_y = 0 \quad \text{(A.5)}$$

Next we assume that the shear forces Q in these equations are negligibly small, leading to the plate equilibrium equations for forces in the planar dimensions presented in Equations A.6 and A.7.

$$\frac{\partial N_x}{\partial x} + \frac{\partial N_{xy}}{\partial y} + F_x = 0 \quad \text{(A.6)}$$

$$\frac{\partial N_y}{\partial y} + \frac{\partial N_{xy}}{\partial x} + F_y = 0 \quad \text{(A.7)}$$

The plate equilibrium equation for the forces in z-direction is obtained in a similar manner and is given by:

$$\frac{\partial Q_x}{\partial x} + \frac{\partial Q_y}{\partial y} + N_x\frac{\partial^2 w}{\partial x^2} + 2N_{xy}\frac{\partial^2 w}{\partial x \partial y} + N_y\frac{\partial^2 w}{\partial y^2} + F_z = 0 \quad \text{(A.8)}$$

For the IPMC element we use a linearized version of the equilibrium equation above, which is given by:

$$\frac{\partial Q_x}{\partial x} + \frac{\partial Q_y}{\partial y} = -F_z \quad \text{(A.9)}$$

A.2 Moment equilibrium equations

Similar to the force equilibria, we begin by taking the sum of moments about the x-axis from the free-body diagram in Figure 2.4 as:

$$-M_x dy + (M_x + dM_x)\, dy - M_{xy}dx + (M_{xy} + dM_{xy})\, dx = 0 \quad \text{(A.10)}$$

Dividing this by $dxdy$ yields the equilibrium equation for the x-direction. The same procedure is used to find the equilibrium equation for the y-direction. Respectively, the moment equilibria about the x- and y-axes are:

$$\frac{\partial M_{xy}}{\partial x} + \frac{\partial M_x}{\partial y} = 0 \tag{A.11}$$

$$\frac{\partial M_y}{\partial x} + \frac{\partial M_{xy}}{\partial y} = 0 \tag{A.12}$$

B Mechanical Stiffness Matrix

B.1 Force Equilibria Weak Form

B.1.1 Force Equilibria In-Plane

Starting from the force equilibrium in x-direction, we derive the weak form of Equation A.6 by integration over the domain Ω and multiplying with test functions ν. The weak form then is:

$$\int_\Omega \frac{\partial N_x}{\partial x}\nu \, d\Omega + \int_\Omega \frac{\partial N_{xy}}{\partial y}\nu \, d\Omega = 0 \tag{B.1}$$

Using the product rule we split each term to obtain:

$$\int_\Omega \frac{\partial}{\partial x}\left(N_x\nu\right) d\Omega - \int_\Omega \frac{\partial \nu}{\partial x}N_x \, d\Omega + \int_\Omega \frac{\partial}{\partial y}\left(N_{xy}\nu\right) d\Omega - \int_\Omega \frac{\partial \nu}{\partial y}N_{xy} \, d\Omega = 0 \tag{B.2}$$

Then, using Gauss' theorem we convert the appropriate terms from integrals over the domain into integrals over the boundary, resulting in:

$$\int_\Gamma \left(N_x\nu\right)\cdot\vec{n} \, d\Gamma - \int_\Omega \frac{\partial \nu}{\partial x}N_x \, d\Omega + \int_\Gamma \left(N_{xy}\nu\right)\cdot\vec{n} \, d\Gamma - \int_\Omega \frac{\partial \nu}{\partial y}N_{xy} \, d\Omega = 0 \tag{B.3}$$

Since boundary conditions are handled in the solver of the FEM framework, we can omit these terms from the PDE for now and obtain:

$$\int_\Omega \frac{\partial \nu}{\partial x}N_x d\Omega + \int_\Omega \frac{\partial \nu}{\partial y}N_{xy} d\Omega = 0 \tag{B.4}$$

Then for the equilibrium in y direction. Starting from Equation A.7, we can derive the force balance in y-direction in weak form in much the same manner as we did for the equilibrium in x-direction. We get:

$$\int_\Omega \frac{\partial \nu}{\partial y}N_y d\Omega + \int_\Omega \frac{\partial \nu}{\partial x}N_{xy} d\Omega = 0 \tag{B.5}$$

B.1.2 Force Equilibrium Out-of-Plane

For the force equilibrium in z-direction, we start from Equation A.9, integrate over the domain and multiply by the test functions to obtain:

$$\int_\Omega \frac{\partial Q_x}{\partial x}\nu \, d\Omega + \frac{\partial Q_y}{\partial y}\nu \, d\Omega = 0 \tag{B.6}$$

We apply the product rule to split the terms and obtain:

$$\int_\Omega \frac{\partial}{\partial x}\left(Q_x\nu\right) d\Omega - \int_\Omega \frac{\partial \nu}{\partial x}Q_x d\Omega + \int_\Omega \frac{\partial}{\partial x}\left(Q_x\nu\right) d\Omega - \int_\Omega \frac{\partial \nu}{\partial y}Q_y d\Omega = 0 \tag{B.7}$$

Then applying Gauss' theorem we convert some of the terms to boundary integrals, yielding:

$$\int_\Gamma \left(Q_x\nu\right)\cdot\vec{n} \, d\Gamma - \int_\Omega \frac{\partial \nu}{\partial x}Q_x d\Omega + \int_\Gamma \left(Q_x\nu\right)\cdot\vec{n} \, d\Gamma - \int_\Omega \frac{\partial \nu}{\partial y}Q_y d\Omega = 0 \tag{B.8}$$

Omitting the boundary terms, we are left with the weak formulation of the out-of-plane force equilibrium as:

$$\int_\Omega \frac{\partial \nu}{\partial x}Q_x d\Omega + \int_\Omega \frac{\partial \nu}{\partial y}Q_y d\Omega = 0 \tag{B.9}$$

B.2 Moment Equilibria Weak Form

The weak form of Equation A.11, the moment equilibrium about the x-axis, is given by integration over the domain and multiplication with the test functions as:

$$\int_\Omega \frac{\partial M_{xy}}{\partial x}\nu \, d\Omega + \int_\Omega \frac{\partial M_x}{\partial y}\nu \, d\Omega = 0 \tag{B.10}$$

Then we apply the product rule to obtain:

$$\int_\Omega \frac{\partial}{\partial x}\left(M_{xy}\nu\right) d\Omega - \int_\Omega \frac{\partial \nu}{\partial x}M_{xy} \, d\Omega + \int_\Omega \frac{\partial}{\partial y}\left(M_x\nu\right) d\Omega - \int_\Omega \frac{\partial \nu}{\partial y}M_x \, d\Omega = 0 \tag{B.11}$$

Next we use Gauss' theorem to convert half of the integrals to boundary integrals, yielding:

$$\int_\Gamma \left(M_{xy}\nu\right)\cdot \vec{n} \, d\Gamma - \int_\Omega \frac{\partial \nu}{\partial x}M_{xy} \, d\Omega + \int_\Gamma \left(M_x\nu\right)\cdot \vec{n} \, d\Gamma - \int_\Omega \frac{\partial \nu}{\partial y}M_x \, d\Omega = 0 \tag{B.12}$$

Since boundary conditions are handled by the solver, we remove the respective integrals from the equation. What remains is the weak formulation of the moment equilibrium about the x-axis:

$$\int_\Omega \frac{\partial \nu}{\partial x}M_x \, d\Omega + \int_\Omega \frac{\partial \nu}{\partial y}M_{xy} \, d\Omega = 0 \tag{B.13}$$

The same steps are repeated to obtain the weak formulation of the moment equilibrium about the y-axis as:

$$\int_\Omega \frac{\partial \nu}{\partial x}M_{xy} \, d\Omega + \int_\Omega \frac{\partial \nu}{\partial y}M_y \, d\Omega = 0 \tag{B.14}$$

B.3 The Mechanical Stiffness Matrix

B.3.1 Mechanical Stiffness Matrix I

We begin the process of obtaining the stiffness matrix by plugging in the definitions of strain ε^0 and curvature κ into Equation 3.24. This is then plugged into the weak form of the force equilibrium in x-direction. This gives us:

$$\begin{aligned}
&\int_\Omega \frac{\partial \nu}{\partial x}\Bigg(A_{11}\frac{\partial u}{\partial x} + A_{12}\frac{\partial v}{\partial y} + A_{16}\left(\frac{\partial u}{\partial y} + \frac{\partial v}{\partial x}\right) + \\
&\qquad B_{11}\left(\frac{\partial \alpha_x}{\partial x} + k_1 q\right) + B_{12}\left(\frac{\partial \alpha_y}{\partial y} + k_2 q\right) + B_{16}\left(\frac{\partial \alpha_x}{\partial y} + \frac{\partial \alpha_y}{\partial x}\right)\Bigg) d\Omega + \\
&\int_\Omega \frac{\partial \nu}{\partial y}\Bigg(A_{16}\frac{\partial u}{\partial x} + A_{26}\frac{\partial v}{\partial y} + A_{66}\left(\frac{\partial u}{\partial y} + \frac{\partial v}{\partial x}\right) + \\
&\qquad B_{16}\left(\frac{\partial \alpha_x}{\partial x} + k_1 q\right) + B_{26}\left(\frac{\partial \alpha_y}{\partial y} + k_2 q\right) + B_{66}\left(\frac{\partial \alpha_x}{\partial y} + \frac{\partial \alpha_y}{\partial x}\right)\Bigg) d\Omega = 0
\end{aligned} \tag{B.15}$$

Next, we move all charge dependent terms to the right-hand side and restructure the terms to obtain:

$$\begin{aligned}
&\int_\Omega \frac{\partial \nu}{\partial x}\left(A_{11}\frac{\partial u}{\partial x} + A_{12}\frac{\partial v}{\partial y} + A_{16}\left(\frac{\partial u}{\partial y} + \frac{\partial v}{\partial x}\right) + B_{11}\frac{\partial \alpha_x}{\partial x} + B_{12}\frac{\partial \alpha_y}{\partial y} + B_{16}\left(\frac{\partial \alpha_x}{\partial y} + \frac{\partial \alpha_y}{\partial x}\right)\right) + \\
&\frac{\partial \nu}{\partial y}\left(A_{16}\frac{\partial u}{\partial x} + A_{26}\frac{\partial v}{\partial y} + A_{66}\left(\frac{\partial u}{\partial y} + \frac{\partial v}{\partial x}\right) + B_{16}\frac{\partial \alpha_x}{\partial x} + B_{26}\frac{\partial \alpha_y}{\partial y} + B_{66}\left(\frac{\partial \alpha_x}{\partial y} + \frac{\partial \alpha_y}{\partial x}\right)\right) d\Omega = \\
&\qquad -q\int_\Omega \frac{\partial \nu}{\partial x}\left(k_1 B_{11} + k_2 B_{12}\right) + \frac{\partial \nu}{\partial y}\left(k_1 B_{16} + k_2 B_{26}\right) d\Omega
\end{aligned} \tag{B.16}$$

With the expanded weak formulation of the force equilibrium in x-direction ready, we exchange the test functions ν with the element shape functions φ_i:

$$\nu = \varphi_i \tag{B.17}$$

Furthermore, we apply the Galerkin method to discretise the degrees of freedom as:

$$u = \sum_{j=0}^{n} u_j \varphi_j, \qquad v = \sum_{j=0}^{n} v_j \varphi_j, \qquad r_x = \sum_{j=0}^{n} \alpha_{x|_j} \varphi_j, \qquad r_y = \sum_{j=0}^{n} \alpha_{y|_j} \varphi_j \tag{B.18}$$

After plugging in and shuffling the terms around, we obtain the discretised force equilibrium in the x-direction as:

$$\begin{aligned}
\sum_{j=1}^{n} \int_\Omega & \left(\frac{\partial \varphi_i}{\partial x} \left(A_{11} \frac{\partial \varphi_j}{\partial x} + A_{16} \frac{\partial \varphi_j}{\partial y} \right) + \frac{\partial \varphi_i}{\partial y} \left(A_{16} \frac{\partial \varphi_j}{\partial x} + A_{66} \frac{\partial \varphi_j}{\partial y} \right) \right) u_j \; + \\
& \left(\frac{\partial \varphi_i}{\partial x} \left(A_{16} \frac{\partial \varphi_j}{\partial x} + A_{12} \frac{\partial \varphi_j}{\partial y} \right) + \frac{\partial \varphi_i}{\partial y} \left(A_{66} \frac{\partial \varphi_j}{\partial x} + A_{26} \frac{\partial \varphi_j}{\partial y} \right) \right) v_j \; + \\
& \left(\frac{\partial \varphi_i}{\partial x} \left(B_{11} \frac{\partial \varphi_j}{\partial x} + B_{16} \frac{\partial \varphi_j}{\partial y} \right) + \frac{\partial \varphi_i}{\partial y} \left(B_{16} \frac{\partial \varphi_j}{\partial x} + B_{66} \frac{\partial \varphi_j}{\partial y} \right) \right) r_{x|_j} + \\
& \left(\frac{\partial \varphi_i}{\partial x} \left(B_{16} \frac{\partial \varphi_j}{\partial x} + B_{12} \frac{\partial \varphi_j}{\partial y} \right) + \frac{\partial \varphi_i}{\partial y} \left(B_{66} \frac{\partial \varphi_j}{\partial x} + B_{26} \frac{\partial \varphi_j}{\partial y} \right) \right) r_{y|_j} d\Omega = \\
-q_i \int_\Omega & \frac{\partial \varphi_i}{\partial x} \left(k_1 B_{11} + k_2 B_{12} \right) + \frac{\partial \varphi_i}{\partial y} \left(k_1 B_{16} + k_2 B_{26} \right) d\Omega
\end{aligned} \tag{B.19}$$

The equation above is part of the system of equations given in Equation 3.1 with the stiffness matrix components on the left hand side, the degrees of freedom part of vector $\mathbf{a}$ and the internal force term on the right-hand side.
Then if follows that the component in x-direction of the displacement stiffness matrix (K_{uu}) becomes:

$$\begin{aligned}
K_{uu,u|_{i,j}} = \sum_{j=0}^{n} \int_\Omega & \frac{\partial \varphi_i}{\partial x} \left(\begin{bmatrix} A_{11} \\ A_{16} \\ 0 \\ B_{11} \\ B_{16} \end{bmatrix}^T \frac{\partial \varphi_j}{\partial x} + \begin{bmatrix} A_{16} \\ A_{12} \\ 0 \\ B_{16} \\ B_{12} \end{bmatrix}^T \frac{\partial \varphi_j}{\partial y} \right) + \\
& \frac{\partial \varphi_i}{\partial y} \left(\begin{bmatrix} A_{16} \\ A_{66} \\ 0 \\ B_{16} \\ B_{66} \end{bmatrix}^T \frac{\partial \varphi_j}{\partial x} + \begin{bmatrix} A_{66} \\ A_{26} \\ 0 \\ B_{66} \\ B_{26} \end{bmatrix}^T \frac{\partial \varphi_j}{\partial y} \right) d\Omega
\end{aligned} \tag{B.20}$$

and the corresponding internal force is:

$$f_{int,u|_i} = -q_i \int_\Omega \frac{\partial \varphi_i}{\partial x} \left(k_1 B_{11} + k_2 B_{12} \right) + \frac{\partial \varphi_i}{\partial y} \left(k_1 B_{16} + k_2 B_{26} \right) d\Omega \tag{B.21}$$

B.3.2 Mechanical Stiffness Matrix II

After substituting Equations 3.24 and the definitions of strain and curvature into the weak formulation of the force equilibrium in y-direction, we apply the Galerkin method as in Equations B.17 and B.18

and rearrange the terms to obtain:

$$\begin{aligned}\sum_{j=1}^{n}\int_{\Omega}\left(\frac{\partial\varphi_i}{\partial y}\left(A_{12}\frac{\partial\varphi_j}{\partial x}+A_{26}\frac{\partial\varphi_j}{\partial y}\right)+\frac{\partial\varphi_i}{\partial x}\left(A_{16}\frac{\partial\varphi_j}{\partial x}+A_{66}\frac{\partial\varphi_j}{\partial y}\right)\right)u_j\ +\\ \left(\frac{\partial\varphi_i}{\partial y}\left(A_{26}\frac{\partial\varphi_j}{\partial x}+A_{22}\frac{\partial\varphi_j}{\partial y}\right)+\frac{\partial\varphi_i}{\partial x}\left(A_{66}\frac{\partial\varphi_j}{\partial x}+A_{26}\frac{\partial\varphi_j}{\partial y}\right)\right)v_j\ +\\ \left(\frac{\partial\varphi_i}{\partial y}\left(B_{12}\frac{\partial\varphi_j}{\partial x}+B_{26}\frac{\partial\varphi_j}{\partial y}\right)+\frac{\partial\varphi_i}{\partial x}\left(B_{16}\frac{\partial\varphi_j}{\partial x}+B_{66}\frac{\partial\varphi_j}{\partial y}\right)\right)r_{x|_j}+\\ \left(\frac{\partial\varphi_i}{\partial y}\left(B_{26}\frac{\partial\varphi_j}{\partial x}+B_{22}\frac{\partial\varphi_j}{\partial y}\right)+\frac{\partial\varphi_i}{\partial x}\left(B_{66}\frac{\partial\varphi_j}{\partial x}+B_{26}\frac{\partial\varphi_j}{\partial y}\right)\right)r_{y|_j}d\Omega=\\ -q_i\int_{\Omega}\frac{\partial\varphi_i}{\partial y}\left(k_1B_{12}+k_2B_{22}\right)+\frac{\partial\varphi_i}{\partial x}\left(k_1B_{16}+k_2B_{26}\right)d\Omega\end{aligned}\tag{B.22}$$

which is part of the system of equations from Equation 3.1. The component in y-direction of the displacement stiffness matrix is then identified as:

$$\begin{aligned}K_{uu,v|_{i,j}}=\sum_{j=0}^{n}\int_{\Omega}\frac{\partial\varphi_i}{\partial y}\left(\begin{bmatrix}A_{12}\\A_{26}\\0\\B_{12}\\B_{26}\end{bmatrix}^T\frac{\partial\varphi_j}{\partial x}+\begin{bmatrix}A_{26}\\A_{22}\\0\\B_{26}\\B_{22}\end{bmatrix}^T\frac{\partial\varphi_j}{\partial y}\right)+\\ \frac{\partial\varphi_i}{\partial x}\left(\begin{bmatrix}A_{16}\\A_{66}\\0\\B_{16}\\B_{66}\end{bmatrix}^T\frac{\partial\varphi_j}{\partial x}+\begin{bmatrix}A_{66}\\A_{26}\\0\\B_{66}\\B_{26}\end{bmatrix}^T\frac{\partial\varphi_j}{\partial y}\right)d\Omega\end{aligned}\tag{B.23}$$

and the corresponding internal force as:

$$f_{int,v|_i}=-kq_i\int_{\Omega}\frac{\partial\varphi_i}{\partial y}\left(k_1B_{12}+k_2B_{22}\right)+\frac{\partial\varphi_i}{\partial x}\left(k_1B_{16}+k_2B_{26}\right)d\Omega\tag{B.24}$$

B.3.3 Mechanical Stiffness Matrix III

The contribution to the mechanical stiffness matrix due to the force equilibrium in z-direction is found by first substituting Equations 3.28 and 2.21 into the weak formulation of the force equilibrium. This yields:

$$\begin{aligned}\int_{\Omega}\frac{\partial\nu}{\partial x}\left(Q_{44}\left(\frac{\partial w}{\partial x}+\alpha_x\right)+Q_{45}\left(\frac{\partial w}{\partial y}+\alpha_y\right)\right)d\Omega+\\ \int_{\Omega}\frac{\partial\nu}{\partial y}\left(Q_{45}\left(\frac{\partial w}{\partial x}+\alpha_x\right)+Q_{55}\left(\frac{\partial w}{\partial y}+\alpha_y\right)\right)d\Omega=0\end{aligned}\tag{B.25}$$

Which we restructure to:

$$\begin{aligned}\sum_{j=1}^{n}\int_{\Omega}\left(\frac{\partial\varphi_i}{\partial x}\left(Q_{44}\frac{\partial\varphi_j}{\partial x}+Q_{45}\frac{\partial\varphi_j}{\partial y}\right)+\frac{\partial\varphi_i}{\partial y}\left(Q_{45}\frac{\partial\varphi_j}{\partial x}+Q_{55}\frac{\partial\varphi_j}{\partial y}\right)\right)w_j+\\ \varphi_j\left(Q_{44}\frac{\partial\varphi_i}{\partial x}+Q_{45}\frac{\partial\varphi_i}{\partial y}\right)\alpha_{x|_j}+\varphi_j\left(Q_{45}\frac{\partial\varphi_i}{\partial x}+Q_{55}\frac{\partial\varphi_i}{\partial y}\right)\alpha_{y|_j}d\Omega=0\end{aligned}\tag{B.26}$$

Next, we identify the contribution to the mechanical stiffness matrix as:

$$K_{uu,w|_{i,j}} = \sum_{j=0}^{n} \int_{\Omega} \frac{\partial \varphi_i}{\partial x} \left(\begin{bmatrix} 0 \\ 0 \\ Q_{44} \\ 0 \\ 0 \end{bmatrix}^T \frac{\partial \varphi_j}{\partial x} + \begin{bmatrix} 0 \\ 0 \\ Q_{45} \\ 0 \\ 0 \end{bmatrix}^T \frac{\partial \varphi_j}{\partial y} + \begin{bmatrix} 0 \\ 0 \\ 0 \\ Q_{44} \\ Q_{45} \end{bmatrix}^T \varphi_j \right) + \frac{\partial \varphi_i}{\partial y} \left(\begin{bmatrix} 0 \\ 0 \\ Q_{45} \\ 0 \\ 0 \end{bmatrix}^T \frac{\partial \varphi_j}{\partial x} + \begin{bmatrix} 0 \\ 0 \\ Q_{55} \\ 0 \\ 0 \end{bmatrix}^T \frac{\partial \varphi_j}{\partial y} + \begin{bmatrix} 0 \\ 0 \\ 0 \\ Q_{45} \\ Q_{55} \end{bmatrix}^T \varphi_j \right) d\Omega \tag{B.27}$$

And, since the right-hand side of Equation B.36 is zero, the internal force term becomes zero as well:

$$f_{int,w|_i} = 0 \tag{B.28}$$

Note that the obtained stiffness matrix component is not only dependent on the derivatived of the shape functions, but also the shape functions themselves directly. This required these components to be integrated in a so-called reduced integration scheme, which effectively reduces the order of the element.

B.3.4 Mechanical Stiffness Matrix IV

For the mechanical stiffness components from the moment equilibrium about the x-axis, we take much the same steps as before. First we plug the definitions of strain and curvature into Equation 3.32 and then substitute that result into the weak formulation of the moment equilibrium. We obtain:

$$\begin{aligned} &\int_{\Omega} \frac{\partial \nu}{\partial x} \Bigg(B_{11} \frac{\partial u}{\partial x} + B_{12} \frac{\partial v}{\partial y} + B_{16} \left(\frac{\partial u}{\partial y} + \frac{\partial v}{\partial x} \right) + \\ &\qquad D_{11} \left(\frac{\partial \alpha_x}{\partial x} + k_1 q \right) + D_{12} \left(\frac{\partial \alpha_y}{\partial y} + k_2 q \right) + D_{16} \left(\frac{\partial \alpha_x}{\partial y} + \frac{\partial \alpha_y}{\partial x} \right) \Bigg) d\Omega + \\ &\int_{\Omega} \frac{\partial \nu}{\partial y} \Bigg(B_{16} \frac{\partial u}{\partial x} + B_{26} \frac{\partial v}{\partial y} + B_{66} \left(\frac{\partial u}{\partial y} + \frac{\partial v}{\partial x} \right) + \\ &\qquad D_{16} \left(\frac{\partial \alpha_x}{\partial x} + k_1 q \right) + D_{26} \left(\frac{\partial \alpha_y}{\partial y} + k_2 q \right) + D_{66} \left(\frac{\partial \alpha_x}{\partial y} + \frac{\partial \alpha_y}{\partial x} \right) \Bigg) d\Omega = 0 \end{aligned} \tag{B.29}$$

Then we move all charge dependent terms to the right-hand side and reorganise the terms, yielding:

$$\begin{aligned} &\int_{\Omega} \frac{\partial \nu}{\partial x} \left(B_{11} \frac{\partial u}{\partial x} + B_{12} \frac{\partial v}{\partial y} + B_{16} \left(\frac{\partial u}{\partial y} + \frac{\partial v}{\partial x} \right) + D_{11} \frac{\partial \alpha_x}{\partial x} + D_{12} \frac{\partial \alpha_y}{\partial y} + D_{16} \left(\frac{\partial \alpha_x}{\partial y} + \frac{\partial \alpha_y}{\partial x} \right) \right) d\Omega + \\ &\int_{\Omega} \frac{\partial \nu}{\partial y} \left(B_{16} \frac{\partial u}{\partial x} + B_{26} \frac{\partial v}{\partial y} + B_{66} \left(\frac{\partial u}{\partial y} + \frac{\partial v}{\partial x} \right) + D_{16} \frac{\partial \alpha_x}{\partial x} + D_{26} \frac{\partial \alpha_y}{\partial y} + D_{66} \left(\frac{\partial \alpha_x}{\partial y} + \frac{\partial \alpha_y}{\partial x} \right) \right) d\Omega = \\ &\qquad - q \int_{\Omega} \frac{\partial \nu}{\partial x} \left(k_1 D_{11} + k_2 D_{12} \right) + \frac{\partial \nu}{\partial y} \left(k_1 D_{16} + k_2 D_{26} \right) d\Omega \end{aligned} \tag{B.30}$$

Next we apply the Galerkin method to dicretise the domain and obtain:

$$\begin{aligned}\sum_{j=1}^{n}\int_{\Omega}\left(\frac{\partial\varphi_i}{\partial x}\left(B_{11}\frac{\partial\varphi_j}{\partial x}+B_{16}\frac{\partial\varphi_j}{\partial y}\right)+\frac{\partial\varphi_i}{\partial y}\left(B_{16}\frac{\partial\varphi_j}{\partial x}+B_{66}\frac{\partial\varphi_j}{\partial y}\right)\right)u_j \quad + \\ \left(\frac{\partial\varphi_i}{\partial x}\left(B_{16}\frac{\partial\varphi_j}{\partial x}+B_{12}\frac{\partial\varphi_j}{\partial y}\right)+\frac{\partial\varphi_i}{\partial y}\left(B_{66}\frac{\partial\varphi_j}{\partial x}+B_{26}\frac{\partial\varphi_j}{\partial y}\right)\right)v_j \quad + \\ \left(\frac{\partial\varphi_i}{\partial x}\left(D_{11}\frac{\partial\varphi_j}{\partial x}+D_{16}\frac{\partial\varphi_j}{\partial y}\right)+\frac{\partial\varphi_i}{\partial y}\left(D_{16}\frac{\partial\varphi_j}{\partial x}+D_{66}\frac{\partial\varphi_j}{\partial y}\right)\right)r_{x|_j}+ \\ \left(\frac{\partial\varphi_i}{\partial x}\left(D_{16}\frac{\partial\varphi_j}{\partial x}+D_{12}\frac{\partial\varphi_j}{\partial y}\right)+\frac{\partial\varphi_i}{\partial y}\left(D_{66}\frac{\partial\varphi_j}{\partial x}+D_{26}\frac{\partial\varphi_j}{\partial y}\right)\right)r_{y|_j}d\Omega = \\ -q_i\int_{\Omega}\frac{\partial\varphi_i}{\partial x}\left(k_1D_{11}+k_2D_{12}\right)+\frac{\partial\varphi_i}{\partial y}\left(k_1D_{16}+k_2D_{26}\right)d\Omega\end{aligned} \tag{B.31}$$

From which we find the contribution to the mechanical stiffness matrix to be:

$$\begin{aligned}K_{uu,\alpha_x|_{i,j}}=\sum_{j=0}^{n}\int_{\Omega}\frac{\partial\varphi_i}{\partial x}\left(\begin{bmatrix}B_{11}\\B_{16}\\0\\D_{11}\\D_{16}\end{bmatrix}^T\frac{\partial\varphi_j}{\partial x}+\begin{bmatrix}B_{16}\\B_{12}\\0\\D_{16}\\D_{12}\end{bmatrix}^T\frac{\partial\varphi_j}{\partial y}\right)+ \\ \frac{\partial\varphi_i}{\partial y}\left(\begin{bmatrix}B_{16}\\B_{66}\\0\\D_{16}\\D_{66}\end{bmatrix}^T\frac{\partial\varphi_j}{\partial x}+\begin{bmatrix}B_{66}\\B_{26}\\0\\D_{66}\\D_{26}\end{bmatrix}^T\frac{\partial\varphi_j}{\partial y}\right)d\Omega\end{aligned} \tag{B.32}$$

and the contribution to the internal force vector to be:

$$f_{int,\alpha_x|_i}=-q_i\int_{\Omega}\frac{\partial\varphi_i}{\partial x}\left(k_1D_{11}+k_2D_{12}\right)+\frac{\partial\varphi_i}{\partial y}\left(k_1D_{16}+k_2D_{26}\right)d\Omega \tag{B.33}$$

B.3.5 Mechanical Stiffness Matrix V

Similarly for the moment equilibrium about the y-axis we begin by substituting Equation 3.32 and the definitions of strain and curvature into the weak formulation of the moment equilibrium about the y-axis. We get:

$$\begin{aligned}\int_{\Omega}\frac{\partial\nu}{\partial x}\Bigg(B_{16}\frac{\partial u}{\partial x}+B_{26}\frac{\partial v}{\partial y}+B_{66}\left(\frac{\partial u}{\partial y}+\frac{\partial v}{\partial x}\right)+ \\ D_{16}\left(\frac{\partial\alpha_x}{\partial x}+k_1q\right)+D_{26}\left(\frac{\partial\alpha_y}{\partial y}+k_2q\right)+D_{66}\left(\frac{\partial\alpha_x}{\partial y}+\frac{\partial\alpha_y}{\partial x}\right)\Bigg)d\Omega+ \\ \int_{\Omega}\frac{\partial\nu}{\partial y}\Bigg(B_{16}\frac{\partial u}{\partial x}+B_{26}\frac{\partial v}{\partial y}+B_{66}\left(\frac{\partial u}{\partial y}+\frac{\partial v}{\partial x}\right)+ \\ D_{12}\left(\frac{\partial\alpha_x}{\partial x}+k_1q\right)+D_{22}\left(\frac{\partial\alpha_y}{\partial y}+k_2q\right)+D_{26}\left(\frac{\partial\alpha_x}{\partial y}+\frac{\partial\alpha_y}{\partial x}\right)\Bigg)d\Omega=0\end{aligned} \tag{B.34}$$

Then we move the charge dependent terms to the right-hand side and reorganise the terms on the left-hand side to obtain:

$$\begin{aligned}\int_\Omega \frac{\partial \nu}{\partial x}\left(B_{16}\frac{\partial u}{\partial x}+B_{26}\frac{\partial v}{\partial y}+B_{66}\left(\frac{\partial u}{\partial y}+\frac{\partial v}{\partial x}\right)+D_{16}\frac{\partial \alpha_x}{\partial x}+D_{26}\frac{\partial \alpha_y}{\partial y}+D_{66}\left(\frac{\partial \alpha_x}{\partial y}+\frac{\partial \alpha_y}{\partial x}\right)\right)d\Omega+\\ \int_\Omega \frac{\partial \nu}{\partial y}\left(B_{12}\frac{\partial u}{\partial x}+B_{22}\frac{\partial v}{\partial y}+B_{26}\left(\frac{\partial u}{\partial y}+\frac{\partial v}{\partial x}\right)+D_{12}\frac{\partial \alpha_x}{\partial x}+D_{22}\frac{\partial \alpha_y}{\partial y}+D_{26}\left(\frac{\partial \alpha_x}{\partial y}+\frac{\partial \alpha_y}{\partial x}\right)\right)d\Omega=\\ -q\int_\Omega \frac{\partial \nu}{\partial x}\left(k_1D_{16}+k_2D_{26}\right)+\frac{\partial \nu}{\partial y}\left(k_1D_{12}+k_2D_{22}\right)d\Omega\end{aligned} \tag{B.35}$$

Which is discretised with the Galerkin method to produce:

$$\begin{aligned}\sum_{j=1}^{n}\int_\Omega &\left(\frac{\partial \varphi_i}{\partial x}\left(B_{16}\frac{\partial \varphi_j}{\partial x}+B_{66}\frac{\partial \varphi_j}{\partial y}\right)+\frac{\partial \varphi_i}{\partial y}\left(B_{12}\frac{\partial \varphi_j}{\partial x}+B_{26}\frac{\partial \varphi_j}{\partial y}\right)\right)u_j \quad +\\ &\left(\frac{\partial \varphi_i}{\partial x}\left(B_{66}\frac{\partial \varphi_j}{\partial x}+B_{26}\frac{\partial \varphi_j}{\partial y}\right)+\frac{\partial \varphi_i}{\partial y}\left(B_{26}\frac{\partial \varphi_j}{\partial x}+B_{22}\frac{\partial \varphi_j}{\partial y}\right)\right)v_j \quad +\\ &\left(\frac{\partial \varphi_i}{\partial x}\left(D_{16}\frac{\partial \varphi_j}{\partial x}+D_{66}\frac{\partial \varphi_j}{\partial y}\right)+\frac{\partial \varphi_i}{\partial y}\left(D_{12}\frac{\partial \varphi_j}{\partial x}+D_{26}\frac{\partial \varphi_j}{\partial y}\right)\right)r_{x|_j}+\\ &\left(\frac{\partial \varphi_i}{\partial x}\left(D_{66}\frac{\partial \varphi_j}{\partial x}+D_{26}\frac{\partial \varphi_j}{\partial y}\right)+\frac{\partial \varphi_i}{\partial y}\left(D_{26}\frac{\partial \varphi_j}{\partial x}+D_{22}\frac{\partial \varphi_j}{\partial y}\right)\right)r_{y|_j}d\Omega=\\ -q_i\int_\Omega &\frac{\partial \varphi_i}{\partial x}\left(k_1D_{16}+k_2D_{26}\right)+\frac{\partial \varphi_i}{\partial y}\left(k_1D_{12}+k_2D_{22}\right)d\Omega\end{aligned} \tag{B.36}$$

From which we are able to find is contribution to the mechanical stiffness matrix as:

$$\begin{aligned}K_{uu,\alpha_y|_{i,j}}=\sum_{j=0}^{n}\int_\Omega &\frac{\partial \varphi_i}{\partial x}\left(\begin{bmatrix}B_{16}\\B_{66}\\0\\D_{16}\\D_{66}\end{bmatrix}^T\frac{\partial \varphi_j}{\partial x}+\begin{bmatrix}B_{66}\\B_{26}\\0\\D_{66}\\D_{26}\end{bmatrix}^T\frac{\partial \varphi_j}{\partial y}\right)+\\ &\frac{\partial \varphi_i}{\partial y}\left(\begin{bmatrix}B_{12}\\B_{26}\\0\\D_{12}\\D_{26}\end{bmatrix}^T\frac{\partial \varphi_j}{\partial x}+\begin{bmatrix}B_{26}\\B_{22}\\0\\D_{26}\\D_{22}\end{bmatrix}^T\frac{\partial \varphi_j}{\partial y}\right)d\Omega\end{aligned} \tag{B.37}$$

and its contribution to the internal force vector of:

$$f_{int,\alpha_y|_i}=-q_i\int_\Omega \frac{\partial \varphi_i}{\partial x}\left(k_1D_{16}+k_2D_{26}\right)+\frac{\partial \varphi_i}{\partial y}\left(k_1D_{12}+k_2D_{22}\right)d\Omega \tag{B.38}$$

C Geometrical instabilities

The validation geometry was designed to include sharp edges to investigate possible numerical instabilities. Due to the nature of the IPMC simulations, mid-plane strains remain small and stress singularities do not occur. The simulations do suffer from another instability: wrinkling. Two cases in which this instability occurs are shown below.

C.1 Potential difference

Firstly, Figure C.1 shows the solution to the potential difference between the electrodes for two slightly differing geometries, based on the verification geometry described in Chapter 4.1.

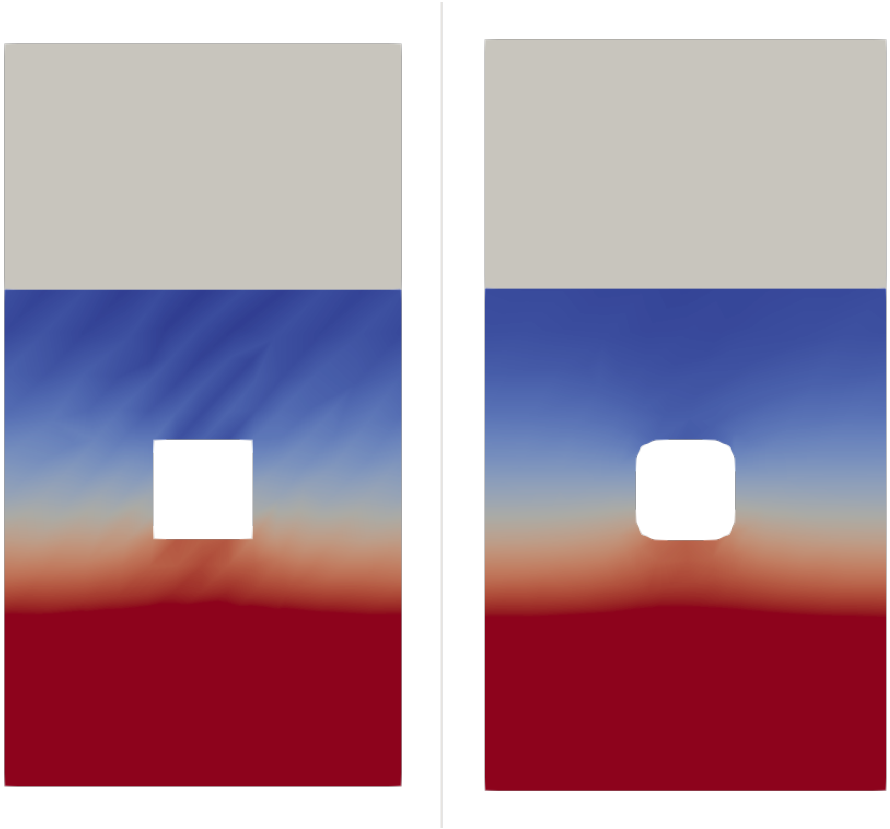

Figure C.1: Wrinkling instability in the potential difference solution alleviated by removing sharp edges in the geometry.

The simulation result on the left shows a wrinkling instability whereas the one on the right doesn't. Through the alleviation of the problem it appears that the sharp edges of the square hole are the culprit of the instability.

Figure C.2 shows a close up of the potential difference solution in the geometry with sharp edges. The color map was adjusted and the mesh is shown for better visualisation.
The figure shows that the wrinkling instability is highly dependent on the shape, size and direction of the elements. The highlighted features show that the wrinkling is mainly propagated on the diagonal from the lower left node to the upper right node. Feature 1. shows a change in wrinkle direction due to a change in mesh directionality. Feature 2. shows a wrinkle failing to propagate along the rib of an element.

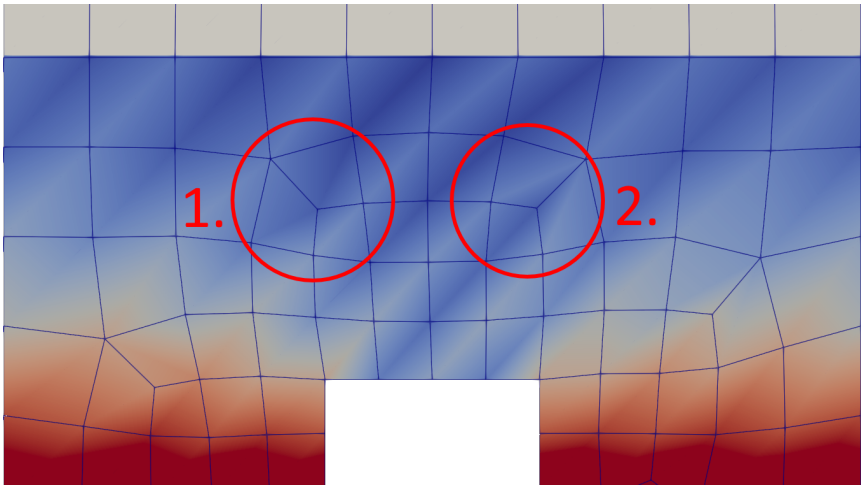

Figure C.2: Wrinkling instability in the potential difference solution is highly mesh dependent.

Figure C.3 shows once more the solution to the potential difference between the electrodes for a near identical simulation. In this simulation a triangular mesh was used instead of the quadrangular mesh on which the wrinkles seemed to propagate so well.
The result is that the wrinkle instability has vanished entirely; likely due to the lack of element diagonals on which to propagate.

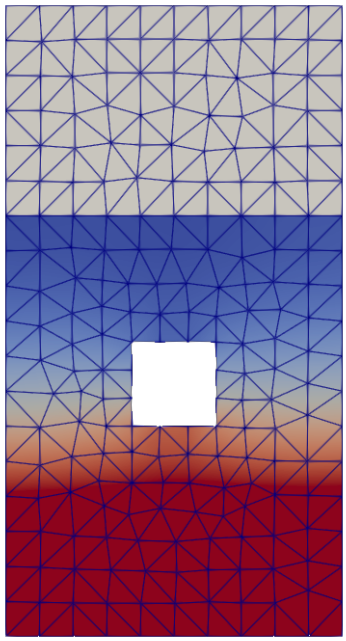

Figure C.3: Wrinkling instability in the potential difference solution alleviated by using triangular mesh.

The wrinkling instabilities in the potential field are caused by using elements with too low of an order of integration. Triangular meshes are more stable than quadrangular meshes and thus allow for a lower order. Any standard linear element with a full integration scheme will not produce this instability, though.

C.2 Displacement

Wrinkling instabilities may also occur due to a geometry being improperly constrained. From the clamped boundary condition we remove only the constraint for out-of-plane displacement on all nodes but the two on the corners of the actuator (highlighted by arrows).
Figure C.4 shows the solution to the displacement magnitude and the severe wrinkling that results; the result is not scaled.

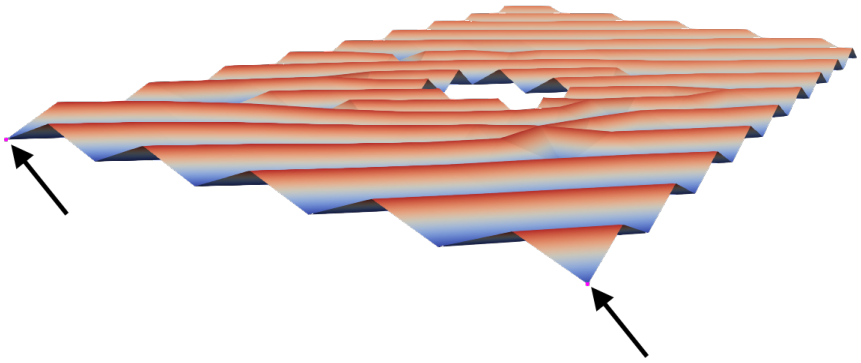

Figure C.4: Wrinkling instability in the potential difference solution is highly mesh dependent.

The problem is remedied as soon as the two out-of-plane constraints on the clamped edge are applied to two nodes of the same element. Alternatively, the wrinkles also disappear when triangular elements are used.